Dissertations of Department of Applied Physics, Helsinki University of Technology
Teknillisen fysiikan laitos, Teknillinen korkeakoulu
Dissertation 156
Espoo 2009

STUDIES OF STATIC AND DRIVEN LATTICE SYSTEMS WITH THE PHASE FIELD CRYSTAL MODEL

Cristian Achim

Dissertation for the degree of Doctor of Science in Technology to be presented with due permission of the Faculty of Information and Natural Sciences for public examination and debate in TKK main building, Otakaari 1, lecture hall E at Helsinki University of Technology (Espoo, Finland) on the 7th of March, 2009, at 13 o'clock.

Helsinki University of Technology
Faculty of Information and Natural Sciences
Department of Applied Physics

Teknillinen korkeakoulu
Informaatio- ja luonnontieteiden tiedekunta
Teknillisen fysiikan laitos

Dissertations of Department of Applied Physics
Helsinki University of Technology
ISSN 1797-9595 (print)
ISSN 1797-9609 (pdf)

Dissertation 156 (2009):
Cristian Achim: Studies of static and driven lattice systems with the Phase Field Crystal model

Opponent:
Laszlo Granasy, Brunel University

ISBN 978-951-22-9775-7 (print)
ISBN 978-951-22-9776-4 (pdf)

Picaset Oy
Helsinki 2009

ABSTRACT OF DOCTORAL DISSERTATION	HELSINKI UNIVERSITY OF TECHNOLOGY P. O. BOX 1000, FI-02015 TKK http://www.tkk.fi

Author Cristian Vasile Achim

Name of the dissertation

Studies of static and driven lattice systems with the Phase Field Crystal model

Manuscript submitted 16.12.2008	Manuscript revised 26.01.2009
Date of the defence 07.03.2009 at 13 o'clock, TKK main building, Otakaari 1, lecture hall E	
☒ Monograph	☐ Article dissertation (summary + original articles)

Faculty	Faculty of Information and Sciences
Department	Department of Applied Physics
Field of research	Computational physics
Opponent(s)	Laszlo Granasy, Brunel University
Supervisor	Tapio Ala-Nissilä
Instructor	Tapio Ala-Nissilä

Abstract

Study of static and dynamical properties of two dimensional lattice systems has become an important topic in nanoscience. Competition between the intrinsic ordering of adsorbed layers and the underlying substrate often leads to the appearance of spatially modulated structures. Important examples include spin density waves, charge density waves, vortex lattices in superconducting films with pinning centers and weakly adsorbed monolayers. In addition to static properties of such systems, their dynamics under external driving force is of great importance in tribology to understand the microscopic origins of friction.

This Thesis deals with the static and dynamic properties of adsorbed layers under the influence of a driving force using an extended version of the Phase Field Crystal Model. In the case of periodic potentials, the various commensurate phases are described in detail and the complete phase diagram is mapped out as a a function of pinning strength and lattice mismatch. For finite temperatures, Monte Carlo simulations are used to determine the phase diagram as a function of temperature. For one of the commensurate phases behavior is found consistent with the Ising universality class. The results concerning the effect of disordered pinning potential are also presented. The nonlinear response to a driving force on an initially pinned commensurate phase is then studied via overdamped dynamic equations of motion for different values of mismatch and pinning strengths. For large pinning strength the driven depinning transitions are continuous, and the sliding velocity varies with the force from the threshold with power-law exponents in agreement with analytical predictions. Transverse depinning transitions in the moving state are also found in two dimensions. Surprisingly, for sufficiently weak pinning potential we find a discontinuous depinning transition with hysteresis even in one dimension under overdamped dynamics. Also, structural changes of the system are characterized in some detail close to the depinning transitions.

Keywords	commensurate-incommensurate transitions, adsorbed layers, depinning, order-disorder transitions	
ISBN (printed)	978-951-22-9775-7	ISSN (printed) 1797-9595
ISBN (pdf)	978-951-22-9776-4	ISSN (pdf) 1797-9609
Language	English	Number of pages 95
Publisher	Department of Applied Physics, Helsinki University of Techology	
Print distribution	Department of Applied Physics, Helsinki University of Techology	

☒ The dissertation can be read at http://lib.tkk.fi/Diss/2009/isbn9789512297764

Preface

The work reported in this thesis was carried out at the Helsinki University of Technology in the Multiscale Statistical Physics group under the supervision of Prof. Tapio Ala-Nissilä. I would like to express my sincere gratitude to him. Without his advise, support and patience this thesis would have never become a reality. Further, I would like to thank our collaborators Ken R. Elder, Enzo Granato, See Chen Ying, Jorge A. P. Ramos and Mikko Karttunen for many fruitful discussions and constructive criticism, which challenged me to improve myself and broaden my knowledge. My office mates and friends, Olli P., Teemu L. and Akusti J., have my gratitude for providing a pleasant and inspiring working environment, and for their open-mindedness. Thanks indeed to all members of the Laboratory of Physics with whom I have interacted in one way or another. The list is simply just too long.

Financial support have been received from National Graduate School in Materials Physics, joint funding under EU STREP Grant No. 016447 MagDot and NSF DMR Grant No. 0502737, the Academy of Finland through its Center of Excellence COMP grant and Magnus Ehrnrooth foundation. Most of the numerical calculations were performed at CSC.

Finally, I would like to thank my family, my friends and my fiancee, Kaia, for all their support and encouragement.

Espoo, March 2009

Cristian

Contents

List of Abbreviations

1D	one dimensional
2D	two dimensional
3D	three dimensional
BCC	body centered cubic
C	commensurate
I	incommensurate
FK	Frenkel-Kontorova
MC	Monte Carlo
PFC	Phase Field Crystal
DFT	Density Functional Theory

List of Figures

1 Introduction

Study of static and dynamical properties of 2D lattice systems has become an important topic in nanoscience. There are many important cases where the behavior of such systems is determined by interplay between various interactions. For example, competition between the intrinsic ordering of an adsorbed layer and the underlying substrate often leads to the appearance of spatially modulated structures. Such systems may exhibit both commensurate (C) and incommensurate (I) phases [51, 5] characterized by differences in the spatial ordering of the system. Important examples include spin density waves [53, 18], charge density waves [47], vortex lattices in superconducting films with pinning centers [30] and weakly adsorbed monolayers [3, 48] on a substrate. The emerging structures are characterized by an order parameter (*e.g.* charge, spin or particle density) that is modulated in space with a given wave vector q. In particular, for 2D adsorbate systems, there is competition between the commensurate state which is favored by a strong periodic pinning potential and the cost of the elastic energy depending on the mismatch between the intrinsic lattice constant a of the overlayer, and the period a_s of the pinning potential.

While the static properties of C and I structures have been extensively characterized [51, 5] much less is known about their dynamics. A particularly interesting case arises when an initially pinned phase is subjected to an external driving force f. For a sufficiently large pinning potential, such phase may remain pinned for small forces if there are no thermal fluctuations present. This means that at zero temperature there is a finite critical force f_c above which the system starts moving. For many systems, it is found that just above the threshold f_c, the drift velocity v_d shows a power-law dependence on the force f

$$v_d \propto (f - f_c)^{\zeta}. \tag{1.1}$$

When this behavior is regarded as a dynamical critical phenomenon, the power-law exponent ζ of the corresponding driven depinning transition can be argued to result from

the scaling behavior of the system near the threshold [20] with corresponding divergent time and length scales and universal behavior. In general, however, the observed value of ζ may depend on the system and its dimensionality. For a pure elastic medium with quenched randomness there appears to be a universal value which depends on the dimensionality of the system, provided inertial effects are negligible [41, 1]. For the case of an initially commensurate phase in a periodic pinning potential without disorder, a power-law exponent $\zeta = 1/2$ is expected independent of the dimension as the threshold behavior can be understood from the point of view of single particle behavior [20, 21, 23, 42]. In the limit of a large force, $(f - f_c)/f_c \gg 1$, the system is moving and the corresponding relationship between the driving force and the sliding velocity defines the sliding friction coefficient

$$\eta_s = f/v_d. \tag{1.2}$$

In addition to the longitudinal depinning transition where the lattice system is moving in the same direction as the driving force, a driven two-dimensional lattice on a periodic potential can also show an interesting behavior for the transverse response in the moving state. When the lattice is already moving along some symmetry direction of the pinning potential, the response to an additional force applied in the direction perpendicular to the longitudinal driving force may lead to a depinning transition for increasing transverse force [16]. Such transverse depinning has been found in different driven lattice systems with periodic pinning including vortex lattices [49] and adsorbed layers [27].

The simple Frenkel-Kontorova (FK) model [37, 13] extended to 2D and other similar elastic models have been used to describe the driven depinning transition and the sliding friction of adsorbed monolayers on crystal surfaces [46, 26]. Although such models take into account topological defects in the form of domain walls they leave out plastic deformations of the layer due to other defects such as dislocations. These defects are particularly important when the CI transition occurs between two different crystal structures, or in the presence of thermal fluctuations or quenched disorder. Such defects can be automatically included in a full microscopic model involving interacting atoms in the presence of a substrate potential using more realistic interaction potentials. However, the full complexities

of the microscopic model severely limit the system sizes that can be studied numerically, even when simple Lennard-Jones potentials are used to describe the interactions [45, 27]. For charge density waves, a field theoretical model has been introduced, which allows for dislocations as well as thermal fluctuations [38] through amplitude and phase fluctuations and shows both elastic and hysteretic behavior in agreement with experiments [36].

When the depinning transition is discontinuous, there are two different critical forces, $f_c^{in} > f_c^{de}$, corresponding to the threshold values for increasing the force from zero and decreasing the force from a large value, respectively. An interesting example is the driven adsorbed layer in a periodic potential which can determine the sliding friction between lubricated surfaces [46]. Hysteresis behavior due to inertial effects can be described by an underdamped dynamical equation of motion using pure elastic models such as the FK model but in the overdamped limit hysteresis disappears [26]. In the absence of inertial effects, hysteresis can be argued to arise from topological defects in the lattice such as dislocations in two-dimensional systems [21]. One thus expects that overdamped dynamics should be able to describe the hysteretic behavior in two-dimensional models which incorporate both elastic and plastic deformations. In fact, hysteresis has been observed in two-dimensional models of driven vortex lattices in a periodic potential, with overdamped dynamics [9]. On the other hand, in one-dimensional driven systems in a periodic potential described by overdamped dynamics one would expect the same behavior as for the pure elastic FK model where the depinning transition is continuous [14].

This Thesis deals with the static and dynamic properties of a two-dimensional lattice system under the influence of an external potential and a driving force. These problems were studied in Refs. [10, 11, 29, 12] by extending the conserved Phase Field Crystal (PFC) model to incorporate the pinning potential and driving force. The pinning potential was chosen such that it allows the occurrence of both C and I phases as ground states of different symmetries in the model. In Ref. [10] part of the phase diagram as function of pinning strength and lattice mismatch between the pinning potential and the PFC was mapped out, for the 2D case, in the absence of thermal fluctuations. Numerical minimization was used

to find the minimum free-energy configurations and provide details on the topological defects in the boundary region. In particular, we found that the transition from the I to the C phase remains discontinuous for all values of the mismatch studied in Ref. [10]. We also performed a detailed Voronoi analysis of the defects throughout the transition region. In Ref. [11] the equilibration method was improved and the range of mismatches extended to include both positive and negative mismatches. The 1D case was presented in Ref. [12]. The transition from I to C phase was found to be discontinuous or continuous depending the relative mismatch. The influence of the thermal fluctuations was studied via Monte Carlo (MC) simulations in Ref. [29]. A modified version of the unconserved PFC model was used to determine the phase diagram as a function temperature and lattice mismatch. The results reveal a rich phase diagram, which includes commensurate, incommensurate, and liquid like phases with a topology dependent on the type of ordered structure. In particular, a finite-size scaling analysis of the melting transition for the c(2×2) commensurate phase shows that the thermal correlation length exponent ν and the specific heat behavior are consistent with the Ising universality class. For the 2D systems preliminary results regarding the influence of a disordered pinning potential are also presented. We study the effect of randomly uniform distributed attractive pinning centers. In the presence of a disordered potential force the system undergoes a transition from a spatially ordered hexagonal state to a spatially disordered state. A continuous transition is found for low density of pinning centers. The orientational order parameter describing the local ordering remains nonzero suggesting the existence of a hexatic phase. The presence of a peak in the dependence of the susceptibility on the pinning strength suggests a continuous phase transition. In the case of high densities of pinning centers the system exhibits an additional continuous transition to an orientationally and spatially disordered phase. Concerning the dynamical properties of driven overlayers, the influence of an external driving force on a commensurate pinned phase was studied for different values of mismatch and pinning strengths for 1D and 2D systems in Ref. [12]. Due to the competition between the pinning potential and the driving force there is a depinning transition at f_c for a finite driving force f. We demonstrated that within a certain range of parameters the depinning transitions are continuous, and find that both in 1D and 2D the corresponding

power-law exponent is $\zeta = 0.5$ in agreement with the expected value [20, 21, 23, 42]. We also characterized structural changes of the system close to the depinning transition. For large pinning strength transverse depinning transitions in the moving state are also found. Surprisingly, for sufficiently weak pinning potential we found a discontinuous depinning transition with hysteresis even in one dimension although overdamped dynamical equations are used.

The Thesis is organized as follows. In Chapter 2 the PFC model is introduced and its basic properties presented for all dimensions following the calculations done in Refs. [17, 54]. Chapter 3 deals with the elastic properties of the PFC model. First we introduced the classical theory of a harmonic crystal and the connections to macroscopic elasticity, as presented in Ref. [4]. Then we show how to calculate the dynamical matrix in the density functional theory (DFT) of freezing as presented in Ref. [40]. In the last part of the Chapter 3 we present a general way to calculate the elastic constants for the PFC model in all dimensions and for any type of Bravais lattice. In Chapter 4 the PFC model is extended to include the effect of external pinning potentials. The static properties of the extended model are presented for both periodic and disordered external potentials. In the first part of Chapter 4, an overview of the results from Refs. [10, 29, 12] concerning the 1D and 2D cases in the presence of periodic potential without thermal fluctuations is presented. The various phases that minimize the free-energy are described in detail and the phase diagrams in terms of the pinning potential strength and periodicity are shown. Next we discuss the results from Ref. [29] regarding the finite temperature behavior of the 2D case of the PFC with external potential. For some of the studied phases, this behavior is consistent with the Ising universality class. At the end of Chapter 4 preliminary results regarding the effect of the disordered potential are presented. Chapter 5 focuses on the results of Ref. [12] regarding the PFC model under an external periodic potential without disorder with an external driving force. The response of the system to the external force is presented for different values of mismatch and pinning strengths for 1D and 2D systems. Although overdamped dynamical equations are used, we find for sufficiently weak pinning potential discontinuous depinning transition with hysteresis in both 1D and

2D cases, while for large values of the pinning strength continuous depinning transitions were found. Also the structural changes of the system close to the depinning transition are presented. In addition, for large pinning strength transverse depinning transitions in the moving state are found. In Chapter 6 we summarize the main results of the Thesis.

2 The Phase Field Crystal Model

Our tool of choice for studying the problems presented in Chapter 1 is the PFC model. The state of the system is described by a continuous density field, $\Phi(\vec{r})$, which is constant for a liquid and forms a periodic pattern in the crystalline phase. Because of this the PFC model incorporates natively elastic and plastic deformations. In the PFC model [17, 35], the free energy functional is written as

$$\mathcal{F}_{\text{SHPFC}} = \int d\vec{r} \left(\frac{a\triangle T}{2}\Phi(\vec{r})^2 + u\frac{\Phi(\vec{r})^4}{4} + \frac{\Phi(\vec{r})}{2}\mathcal{G}(\nabla^2)\Phi(\vec{r}) \right), \tag{2.1}$$

where $\mathcal{G}(\nabla^2) = \lambda\left(k_0^2 q_0^2 + \nabla^2\right)^2$ and $a\Delta T$ represents the mean-field temperature. Eq. (2.1) describes a crystal with the first reciprocal vector of magnitude $k_0 q_0$ (k_0 is the magnitude of first reciprocal lattice when the distances are measured in units of $1/q_0$), while the elastic properties can be adjusted by λ, u and $k_0 q_0$. The parameters of the model can be fitted to reproduce the lattice constant and the desire property (elastic constants, surface energy or the relative solidification miscibility gap) of the material studied.

Version (2.1) of the model is also called Swift-Hohenberg PFC model. The PFC model can be derived as an approximation of the Density Functional Theory (DFT) of freezing as demonstrated in Appendix A. The properties of the PFC model for the 1D and 2D cases were presented in Ref. [17], while the 3D case in Ref. [54]. In this chapter we present the basic properties of the PFC model in all dimensions, following the calculations done in Refs. [17] and [54].

For numerical calculations it is convenient to rewrite the free energy in dimensionless units [17] as

$$\vec{x} = \vec{r}q_0, \psi = \Phi\sqrt{\frac{u}{\lambda q_0^4}}, r = \frac{a\triangle T}{\lambda q_0^4}, \tau = \Gamma\lambda q_0^4 t. \tag{2.2}$$

In these units the free energy becomes

$$F = \frac{\mathcal{F}}{\lambda^2 q^{8-d}/u} = \int d\vec{x} \left[\frac{\psi(\vec{x})}{2}\omega\left(\nabla^2\right)\psi(\vec{x}) + \frac{\psi(\vec{x})^4}{4} \right], \tag{2.3}$$

where $\omega\left(\nabla^2\right) = r + \left(k_0^2 + \nabla^2\right)^2$. Since ψ is a conserved field it must obey the equation of continuity in which the flux term is $\nabla \cdot \vec{j} = \nabla^2(\delta F/\delta\psi)$,

$$\frac{\partial\psi(\vec{x})}{\partial\tau} = \nabla^2\frac{\delta F}{\delta\psi(\vec{x})} + \zeta = \nabla^2\left(\omega\left(\nabla^2\right)\psi(\vec{x}) + \psi(\vec{x})^3\right) + \zeta(\vec{x}), \tag{2.4}$$

where ζ has zero mean, $\left\langle\zeta\left(\vec{x}_1,\tau_1\right)\zeta\left(\vec{x}_2,\tau_2\right)\right\rangle = \mathcal{D}\nabla^2\delta\left(\vec{x}_1 - \vec{x}_2\right)\delta\left(\tau_1 - \tau_2\right)$ and $\mathcal{D}$ is a constant. Equations (2.3) and (2.4) have been used to study a variety of phenomena with elastic and plastic deformation including grain boundary energies between misaligned grains, buckling and dislocation nucleation in liquid phase epitaxial growth, the reverse Hall-Petch effect in nano-crystalline materials and grain growth and ductile fracture [17].

In the absence of an external potential, the state of the system depends on the value of the average density $\bar{\psi} = 1/V_d\int_{V_d} d\vec{x}\psi(\vec{x})$ (V_d is the d dimensional volume) and the mean-field temperature r. The free energy defined by Eq. (2.3) is minimized by constant ('liquid') or period ('solid') solutions [17]. In the liquid phase the density is constant in space

$$\psi(\vec{x}) = \bar{\psi}, \tag{2.5}$$

and the free energy obtained by inserting this solution in Eq. (2.3) is

$$F_c/V_d = \frac{1}{2}(r + k_0^4)\bar{\psi}^2 + \frac{1}{4}\psi^4. \tag{2.6}$$

A general solution of the periodic phases can be written expanded in Fourier series as

$$\psi(\vec{x}) = \sum_{\vec{G}} a_{\vec{G}}e^{i\vec{G}\cdot\vec{x}} + \bar{\psi}, \tag{2.7}$$

where the sum is performed over the relevant reciprocal vectors $\vec{G}$ of the crystalline phase. In a one-mode approximation only the vectors with magnitude equal to the first reciprocal lattice vector are considered.

2.1 One dimension

In addition to the constant phase the free energy can be minimized by a periodic phase which is written in a one-mode approximation as [17]

$$\psi(x) = A_p \cos(k_p x) + \bar{\psi}, \tag{2.8}$$

where k_p and A_p must be chosen so that the energy is minimized. The wave number k_p is related to the lattice constant of the periodic phase a_p through the relation $k_p = 2\pi/a_p$. After inserting this form of the density in Eq. (2.3) we obtain

$$F_p(A_p, k_p, r, \bar{\psi})/L = \frac{1}{4}A_p^2(3\bar{\psi}^2 + r + (k_0^2 - k_p^2)^2) + \frac{3}{32}A_p^4 + F_c/L, \tag{2.9}$$

where L is the size of the system. In order to minimize the free energy the wave vector k_p must be equal to k_0, while the amplitude A_p is given by

$$A_p^2 = -4(\frac{1}{3}r + \bar{\psi}^2). \tag{2.10}$$

We can see that the periodic phase can exist only for $r < -3\bar{\psi}^2$. The free energy of the periodic phase will then be

$$F_p^{\min}(r, \bar{\psi})/L = -(1/6)r^2 + (1/2)(k_0^4 - r)\bar{\psi}^2 - (5/4)\bar{\psi}^4 \tag{2.11}$$

The phase diagram is determined comparing this energy with that of the constant phase, F_c. The Maxwell equal-area construction rule must be satisfied in order to obtain equilibrium states *i.e.*

$$\int_{\bar{\psi}_1}^{\bar{\psi}_2} d\bar{\psi}[\mu(\bar{\psi}) - \mu_{eq}] = 0, \tag{2.12}$$

where $\mu(\bar{\psi}) = \mu_p = \partial F_p^{\min}/\partial\bar{\psi}$ ($\mu(\bar{\psi}) = \mu_c = \partial F_c/\partial\psi$) if $F_p^{\min} < F_c$ ($F_p^{\min} > F_c$), $\bar{\psi}_1$ is solution of $\mu_p = \mu_{eq}$ and and $\bar{\psi}_2$ is solution of $\mu_c = \mu_{eq}$. The phase transition between the constant and periodic phases is of first order, i.e. regions of coexistence are present. The phase diagram of the 1D PFC model calculated in Ref. [17] is shown in Fig 2.1(a).

It is also possible to calculate in the elastic energy using in the one-mode approximation as a function of the strain $u = (a_p - a_0)/a_0$, where $a_0 = 2\pi/k_0$. For a small change of

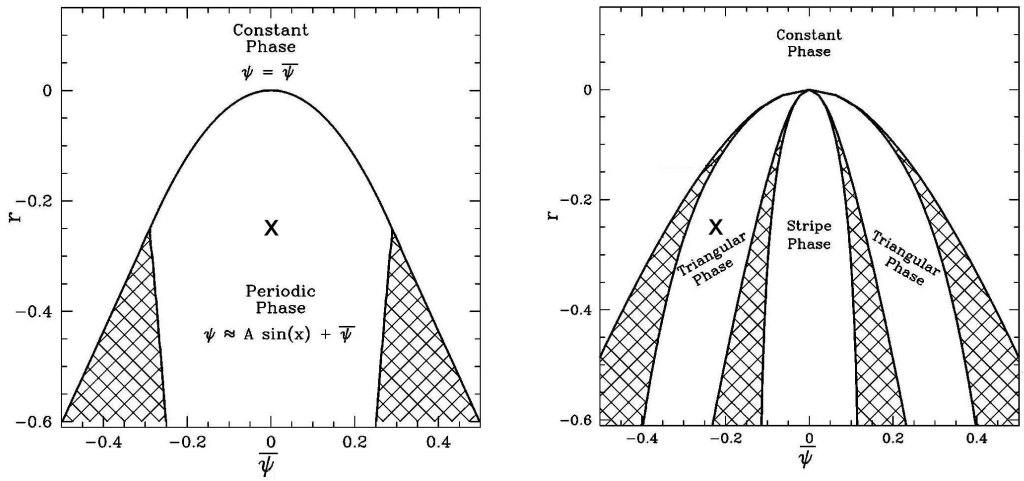

(a) (b)

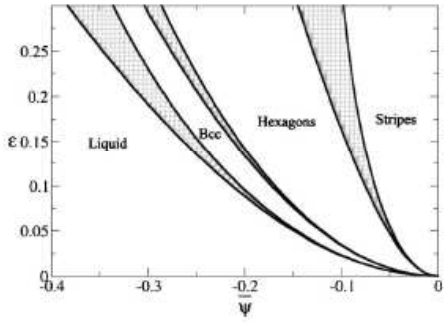

(c)

Figure 2.1: (a) 1D and (b) 2D phase diagrams calculated analytically in Ref. [17] using one-mode approximation and (c) 3D phase diagram (calculated in Ref. [54]), where the parameter $\epsilon = -r$. The solid line is the boundary separating constant different phases. The hatched section of the plots corresponds to regions of coexistence between the phases. For the discussion of the 2D and 3D cases see Secs. 2.2 and 2.3.

the lattice constant a_p the total energy is

$$F_p/L = F_p^{\min}/L + K\frac{u^2}{2} + \mathcal{O}(u^3), \tag{2.13}$$

where $K = 2A_p^2 k_0^4$ is the bulk modulus and $A_p^2 = -4((1/3)r + \bar{\psi}^2)$.

2.2 Two dimensions

In 2D systems, there are two periodic phases: stripes and triangular. The free energy of the stripes is identical to the one-dimensional periodic phase. In Ref. [17] the one-mode approximation for the triangular phase is obtained from Eq. (2.7) by restricting the sum to the reciprocal lattice vectors of magnitude k_t. For a triangular lattice with lattice constant a_t the reciprocal lattice vectors are $\vec{G} = n\vec{b}_1 + m\vec{b}_2$, where

$$\begin{aligned} \vec{b}_1 &= k_t \left(\frac{\sqrt{3}}{2}\hat{x} + \frac{1}{2}\hat{y} \right), \\ \vec{b}_2 &= k_t \hat{y}, \end{aligned} \tag{2.14}$$

with $k_t = 2\pi/(a_t\sqrt{3}/2)$. For the one-mode approximation six pairs (n, m) are taken into account, namely $(0, \pm 1), (\pm 1, 0), (-1, 1)$ and $(1, -1)$, for which $|\vec{G}| = k_t$. Considering the symmetry of the lattice and the fact that the density is real, all the amplitudes $a_{\vec{G}}$ are equal for the given pairs (n, m). Thus, the density can be expressed in the one-mode approximation as

$$\psi_t(\vec{x}) = A_t \left(\cos\left(\frac{\sqrt{3}}{2} k_t x \right) \cos\left(\frac{1}{2} k_t y \right) - \frac{1}{2} \cos\left(k_t y \right) \right) + \bar{\psi}, \tag{2.15}$$

where A_t and k_t are to be determined by minimizing the free energy. Substituting Eq. (2.15) in Eq. (2.3) and integrating in space gives

$$F_t/S = \frac{45}{512} A_t^4 - \bar{\psi}\frac{3}{16} A_t^3 + \frac{3}{16}\left(3\bar{\psi} + r + (k_0^2 - k_t^2)^2 \right) A_t^2 + F_c/S, \tag{2.16}$$

where S is the area of the system. The free energy is minimized by $k_t = k_0$ and $A_t = (4/5)\left(\bar{\psi} + \text{sign}(\bar{\psi})\sqrt{-36\bar{\psi}^2 - 15r} \right)$, where $\text{sign}(\bar{\psi}) = -1$ for $\bar{\psi} < 0$ and $\text{sign}(\bar{\psi}) = 1$ for $\bar{\psi} > 0$. The free energy of the triangular phase is

$$\begin{aligned} F_t^{\text{min}}/S &= -\frac{13}{500}\bar{\psi}^4 - \frac{1}{10} r^2 + \frac{1}{2}(\frac{7}{25} r + k0^4)\bar{\psi}^2 && (2.17) \\ &+ \frac{4}{25}|\bar{\psi}|(\frac{4}{5}\bar{\psi}^2 + \frac{1}{3} r)\sqrt{-36\bar{\psi}^2 - 15r}. && (2.18) \end{aligned}$$

To determine the phase diagram, the energies of the different phase (stripes, triangular and constant) are compared. In addition, since ψ is a conserved field, the Maxwell equal

area construction must be done in order to find the coexistence regions. The results of these calculations are shown in Fig. 2.1(b) [17].

The elastic properties of the triangular phase can be obtained by calculating the costs for deforming the equilibrium state. In two dimensions several types of deformations are considered by applying modified forms of Eq. (2.15) —i.e. $\psi_t(x/(1+\epsilon)), y/(1+\epsilon))$ (bulk), $\psi_t(x+\epsilon y, y)$ (shear), and $\psi_t(x(1-\epsilon), y(1+\epsilon))$ (deviatoric). In the calculations ϵ represents the dimensionless deformation. The results from the calculation performed in Ref. [17] are:

$$\begin{aligned} F_{bulk}/S &= F_t^{\min}/S + \alpha\epsilon^2 + \ldots, \\ F_{shear}/S &= F_t^{\min}/S + (\alpha/8)\epsilon^2 + \ldots, \\ F_{deviatoric}/S &= F_t^{\min}/S + (\alpha/2)\epsilon^2 + \ldots, \end{aligned} \tag{2.19}$$

with $\alpha = (3A_t^2 k_0^4)/4$. Using these results the elastic constants can be calculated taking into account that, for a two dimensional system [13]

$$\begin{aligned} F_{bulk}/S &= F_t^{\min}/S + (C_{11}+C_{12})\epsilon^2 + \ldots, \\ F_{shear}/S &= F_t^{\min} + (C_{44}/2)/S\epsilon^2 + \ldots, \\ F_{deviatoric}/S &= F_t^{\min}/S + (C_{11}-C_{12})\epsilon^2 + \ldots, \end{aligned} \tag{2.20}$$

The elastic constants are then given by

$$C_{11}/3 = C_{12} = C_{44} = \alpha/4 \tag{2.21}$$

These results are consistent with the symmetries of the two dimensional triangular system —i.e. $C_{11} = C_{12} + 2C_{44}$, but this model is restricted to materials with $C_{11} = 3C_{12}$. In the free energy the parameters can be chosen to produce any C_{11}, but C_{12} can not be varied independently. With these results the standard elastic moduli and constants can be determined:

Bulk modulus	$B = \alpha/2$
Shear modulus	$\mu = \alpha/4$
Young's modulus	$Y_{2d} = 3\alpha/3$
Poisson's ration	$\sigma = \frac{1}{3}$.

While these results are consistent with the symmetries of the two dimensional triangular system and the parameters can be chosen to reproduce the elastic moduli of an experimental systems, it should be noted that in this simplistic model the Poisson's ration is always $\sigma = 1/3$ (in one-mode approximation). The accuracy of these approximations for the bulk modulus was tested by numerical calculations and the agreement was found to be quite good in the limit of small r [17].

2.3 Three dimensions

The properties of the 3D PFC model were presented in Ref. [54]. In 3D the periodic phases that minimize the free energy are: hexagonal patterns of tubes with an energy identical to the triangular phase, periodic walls with energy identical to the 1D periodic phase, and the body centered cubic (BCC) phase, which is expressed in the one-mode approximation as

$$\begin{aligned} \psi_{BCC}(\vec{x}) &= \bar{\psi} + A_{BCC}(\cos(k_{BCC}x/\sqrt{2})\cos(k_{BCC}y(\sqrt{2}) \\ &+ \cos(k_{BCC}y/\sqrt{2})\cos(k_{BCC}z/\sqrt{2}) + \cos(k_{BCC}z/\sqrt{2})\cos(k_{BCC}x/\sqrt{2}), \end{aligned} \tag{2.22}$$

where V is the volume, the amplitude A_{BCC} is a parameter to be determined and k_{BCC} is the magnitude of the smallest reciprocal lattice vector. The lattice constant of the BCC phase is $a_{BCC} = 2\pi\sqrt{2}/k_{BCC}$. The energy in the one-mode approximation is

$$F_{BCC}/V = \frac{135}{256}A_{BCC}^4 + \frac{3}{4}A_{BCC}^3\bar{\psi} + \frac{3}{8}A_{BCC}^2(3\bar{\psi}^2 + r + (k_0^2 - k_{BCC}^2)^2) + F_c/V, \tag{2.23}$$

where A_{BCC} and k_{BCC} must minimize the free energy. The free energy is minimized by $k_{BCC} = k_0$ and $A_{BCC} = -\bar{\psi}(4/15)(2 + \text{sign}(\bar{\psi})\sqrt{-11\bar{\psi}^2 - 5r})$, and thus the solution for a BCC structure exist only for $11\bar{\psi}^2 < -5r$. The free energy of the BCC phase is then

$$\begin{aligned} F_{BCC}/V &= \frac{16}{225}|\bar{\psi}|(r + \frac{11}{5}\bar{\psi}^2)\sqrt{-11\bar{\psi}^2 - 5r} \\ &- \frac{1}{15}r^2 + \frac{793}{4500}\bar{\psi}^4 + \frac{47}{150}r\bar{\psi}^2 + \frac{1}{2}k_0^4\bar{\psi}^2 \end{aligned} \tag{2.24}$$

Comparing the free-energies of the different phases (BCC, constant, hexagonal tubes and periodic walls) and taking into account the Maxwell equal area construction, the phase diagram was computed. Fig 2.1(c) shows the full phase diagram of the 3D PFC model calculated in Ref. [54], where the parameter $\epsilon = -r$.

The bulk modulus can be calculated by considering deformations of the form $\psi(\vec{x}/(1+\epsilon))$ and expanding the free energy in ϵ to obtain

$$B = \frac{3k_0^4}{2} A_{BCC}^2. \tag{2.25}$$

In the next section it will be demonstrated how to calculate the elastic constants of the PFC model, from the dynamical matrix.

3 Dynamical matrix and elastic constant tensor in the PFC model

The PFC free energy depends only on three parameters, which can be fit to reproduce certain features, such as relative fraction of freezing, surface energy in the liquid-solid coexistence or elastic constants. In this chapter we will give a brief introduction to the classical theory of harmonic crystal and show how to calculate the harmonic contribution to the energy and the connection to elasticity in the harmonic approximation, as presented in Ref. [4]. Then it is shown how to calculate the dynamical matrix in DFT of freezing as presented in Ref. [40]. In the last part of this chapter the dynamical matrix and elastic constants of the PFC model are calculated and results for the hexagonal and BCC lattice are presented.

3.1 Distortion energy of a mono-atomic Bravais lattice

Many condensed systems form crystalline solid phases which consist of units (atoms, molecules, or ions) arranged in an orderly repeating pattern extending in all spatial dimensions. The periodic pattern in which the units are arranged is called a Bravais lattice [4, 13]. For a d dimensional crystal, any lattice point can be specified by a linear combination of d independent translation vectors, $\vec{a}_1, \ldots, \vec{a}_d$:

$$\vec{R} = n_1\vec{a}_1 + n_2\vec{a}_2 + \ldots + n_d\vec{a}_d. \tag{3.1}$$

In coordinate space the lattice of points is often called the direct lattice. Reciprocal lattice is the set of all vectors $\vec{G}$ such that:

$$\vec{G}_i \cdot \vec{a}_j = 2\pi\delta_{ij}, \tag{3.2}$$

where $i, j = 1, \ldots, d$.

The potential energy of a crystal consisting of N_p particles interacting via a pair wise potential, in equilibrium with each other, is just the sum of all possible pairs:

$$U = \frac{1}{2}\sum_{\vec{R},\vec{R}'} \tilde{\Phi}(\vec{R} - \vec{R}'). \tag{3.3}$$

However at finite temperature the atoms are oscillating around the equilibrium positions $\vec{R}_j$ with the typical displacements $\vec{u}(\vec{R}) = \vec{r}(\vec{R}) - \vec{R}$ (which are are small compared to the interatomic spacing) and the potential energy (3.3) must be replaced by

$$U = \frac{1}{2}\sum_{\vec{R},\vec{R}'} \tilde{\Phi}(\vec{R} - \vec{R}' + \vec{u}(\vec{R}) - \vec{u}(\vec{R}')). \tag{3.4}$$

Even for a simple pair potential like the Lennard-Jones case, extracting useful information from the energy (3.4) is a hopeless task and we must use approximations, based on the expectation that the atoms will not deviate substantially from the equilibrium positions [4]. For small displacements $\vec{u}(\vec{R})$ the energy (3.4) can be expanded in Taylor series around the equilibrium value [4]

$$\begin{aligned} U &= \frac{1}{2}\sum_{\vec{R},\vec{R}'} \tilde{\Phi}(\vec{R} - \vec{R}') + \frac{1}{2}\sum_{\vec{R},\vec{R}'} (\vec{u}(\vec{R}) - \vec{u}(\vec{R}')) \cdot \nabla\tilde{\Phi}(\vec{R} - \vec{R}') \\ &+ \frac{1}{4}\sum_{\vec{R},\vec{R}'} [(\vec{u}(\vec{R}) - \vec{u}(\vec{R}') \cdot \nabla]^2 \tilde{\Phi}(\vec{R} - \vec{R}') + \mathcal{O}(u^3). \end{aligned} \tag{3.5}$$

Because the expansion is done around the equilibrium, the coefficient of $(\vec{u}(\vec{R}) - \vec{u}(\vec{R}'))$ in the linear term, $\nabla\tilde{\Phi}(\vec{R} - \vec{R}')$, must vanish, since there is no net force on any atom in equilibrium. In the harmonic approximation [4] only the quadratic term is retained from the expansion and the energy can be written as

$$U = U^{eq} + U^{harm}, \tag{3.6}$$

where U^{eq} is the equilibrium energy (3.3) and

$$\begin{aligned} U^{harm} &= \frac{1}{4}\sum_{\vec{R},\vec{R}',\alpha,\beta=x,y,z} [u_\alpha(\vec{R}) - u_\alpha(\vec{R}')]\tilde{\Phi}_{\alpha\beta}(\vec{R} - \vec{R}')[u_\beta(\vec{R}) - u_\beta(\vec{R}')]; \\ \tilde{\Phi}_{\alpha\beta}(\vec{r}) &= \frac{\partial^2\tilde{\Phi}(\vec{r})}{\partial r_\alpha \partial r_\beta}. \end{aligned} \tag{3.7}$$

Eq. (3.7) can be recast in a more convenient form as

$$U^{harm} = \frac{1}{2} \sum_{\vec{R},\vec{R}',\alpha,\beta} u_\alpha(\vec{R}) D_{\alpha\beta}(\vec{R} - \vec{R}') u_\beta(\vec{R}'), \tag{3.8}$$

where $D_{\alpha\beta}(\vec{R}-\vec{R}') = \delta_{\vec{R}\vec{R}'} \sum_{\vec{R}''} (\tilde{\Phi}_{\alpha\beta}(\vec{R}-\vec{R}'') - \tilde{\Phi}_{\beta\alpha}(\vec{R}-\vec{R}'))$. Regardless of the particular forms of the interatomic forces there are several symmetries that the matrix $D_{\alpha\beta}(\vec{R}-\vec{R}')$ must obey [4]: $D_{\alpha\beta}(\vec{R}-\vec{R}') = D_{\beta\alpha}(\vec{R}-\vec{R}')$ (because $D_{\alpha\beta}(\vec{R}-\vec{R}') = \frac{\partial^2 U}{\partial u_\alpha(\vec{R}) \partial u_\beta(\vec{R}')}$ and the independence of the order of the differentiation), $D_{\alpha\beta}(\vec{R}) = D_{\alpha\beta}(-\vec{R})$ (because the Bravais lattice has inversion symmetry), and $\sum_{\vec{R}} D_{\alpha\beta}(\vec{R}) = 0$ (if each ion is given the same displacement, i.e. $\vec{u}(\vec{R}) = \vec{d}$, for all $\vec{R}$, the crystal is simply displaced without any internal distortion).

The *dynamical matrix* $D_{\alpha\beta}(\vec{q})$ is the Fourier transform of the matrix $D_{\alpha\beta}(\vec{R})$,

$$D_{\alpha\beta}(\vec{q}) = \sum_{\vec{R}} D_{\alpha\beta}(\vec{R}) e^{-i\vec{q}\cdot\vec{R}}, \tag{3.9}$$

where $\vec{q}$ is restricted to the first Brillouin zone [13, 4]. The harmonic potential is

$$U^{harm} = \frac{1}{2} \int \frac{d^d q}{2\pi^d} \sum_{\alpha,\beta} D_{\alpha\beta}(\vec{q}) \hat{u}_\alpha(\vec{q}) \hat{u}_\beta(\vec{q}), \tag{3.10}$$

where $\hat{u}_\alpha = \sum_{\vec{R}} u_\alpha(\vec{R}) e^{i\vec{q}\cdot\vec{R}}$ and $D_{\alpha\beta}(\vec{q}) = \sum_{\mu\nu} K_{\alpha\mu\beta\nu} q_\mu q_\nu$ [13]. $K_{\alpha\mu\beta\nu} q_\mu q_\nu$ is the elastic constant tensor. By knowing the dynamical matrix and studying the long-wave behavior we can calculate the elastic constants for different Bravais lattices. The eigenvalues of the dynamical matrix give the phonon spectrum, $\omega(\vec{q})$

$$\omega^2 \hat{u}_\alpha = \sum_\beta D_{\alpha\beta} \hat{u}_\beta(\vec{q}). \tag{3.11}$$

Phonon spectra are known for a large number of materials. Calculating the dynamical matrix for a specific model gives the possibility to use experimental data as an input, when elastic properties are relevant.

In the next section we will demonstrate how to calculate the dynamical matrix within the DFT of freezing starting from the free-energy functional, following the calculations made in Ref. [40].

3.2 Distortion energy in the DFT theory of freezing

In the classical DFT of freezing [52] the free energy of the solid phase is written as perturbation around a reference liquid state at the melting transition

$$\begin{aligned} \frac{\mathcal{F}_{\rm DFT}}{k_BT} &= \int d\vec{x}\,[\rho(\vec{x})\log(\rho(\vec{x})/\rho_l)-\delta\rho(\vec{x})] \\ &- (1/2)\int d\vec{x}d\vec{x}'\delta\rho(\vec{x})C(\vec{x}-\vec{x}')\delta\rho(\vec{x}'), \end{aligned} \tag{3.12}$$

where $C(\vec{x}-\vec{x}')$ is the direct two point correlation function measured in the reference liquid and $\delta\rho(\vec{x})-\rho_l$. We can write the density, $\rho_0(\vec{x})$, that minimizes the free energy (3.12) for the constraint $(1/V_d)\int d\vec{x}\rho(\vec{x})=\bar{\rho}$ as

$$\rho_0(\vec{x})=\bar{\rho}+\sum_{\vec{G}\neq 0}\hat{\rho}_0(\vec{G})e^{i\vec{G}\cdot\vec{x}}. \tag{3.13}$$

More generally, we can write the fluctuating density [40] in the form

$$\rho(\vec{x})=\bar{\rho}+\sum_{\vec{G}\neq 0}\hat{\mu}_{\vec{G}}(\vec{x})e^{i\vec{G}\cdot\vec{x}}. \tag{3.14}$$

When looking at distances large compared to a lattice spacing, we can assume that the amplitude $\hat{\mu}_{\vec{G}}(\vec{x})$ in terms of the Fourier amplitude of the equilibrium density and a complex phase [40],

$$\hat{\mu}_{\vec{G}}(\vec{x})=\hat{\rho}_0(\vec{G})e^{i\vec{G}\cdot\vec{u}(\vec{x})}, \tag{3.15}$$

where $\vec{u}(\vec{x})$ plays the role of a displacement field. In the case of slowly varying and small displacement the density $\rho(x)$ can be extended in powers of $\vec{u}(\vec{x})$ [40],

$$\begin{aligned} \rho(\vec{x}) &= \rho_0(\vec{x})+(\nabla\rho_0(\vec{x}))\cdot\vec{u}(\vec{x})+\ldots; \\ \rho(\vec{x}) &\equiv \rho_0(\vec{x})+\Delta\rho(\vec{x}). \end{aligned} \tag{3.16}$$

The harmonic part of the free energy is

$$\frac{\mathcal{F}^{harm}_{\rm DFT}}{k_BT}=\frac{1}{2}\int d\vec{x}_1d\vec{x}_2\frac{\delta^2\mathcal{F}_{\rm DFT}}{\delta\rho(\vec{x}_1)\delta\rho(\vec{x}_2)}|_{\rho=\rho_0}\Delta\rho(\vec{x}_1)\Delta\rho(\vec{x}_2), \tag{3.17}$$

where the second order derivative of the free energy is given by

$$\frac{\delta^2\mathcal{F}_{\rm DFT}}{\delta\rho(\vec{x}_1)\delta\rho(\vec{x}_2)}|_{\rho=\rho_0}=\frac{\rho_l}{\rho_0(\vec{x})}\delta(\vec{x}_1-\vec{x}_2)-C(\vec{x}_1-\vec{x}_2). \tag{3.18}$$

Using the Fourier expansion of $\rho_0(\vec{x})$ and $\vec{u}(r) = \sum_{\vec{q}} \hat{\vec{u}}(\vec{q}) e^{i\vec{q}\cdot\vec{x}}$, with $\vec{q}$ restricted to the first Brillouin zone [4], and performing the integration with respect to spatial variables we obtain

$$\begin{aligned} \int d\vec{x}_1 d\vec{x}_2 \Delta\rho(\vec{x}_1)\Delta\rho(\vec{x}_2)C(\vec{x}_1-\vec{x}_2) &= \sum_{\vec{G}\vec{G}'\vec{q}\vec{q}'\alpha\beta} \rho_0(\vec{G})\rho_0(\vec{G}')\hat{c}((\vec{G}'+\vec{q}')^2) \times \\ &\times \ (i\vec{G}_\alpha)(i\vec{G}'_\beta)\hat{u}_\alpha(\vec{q})\hat{u}_\beta(\vec{q}')V\delta_{\vec{G}+\vec{G}'+\vec{q}+\vec{q}',0}, \end{aligned} \tag{3.19}$$

with $\hat{c}((\vec{k})^2) = \int d\vec{x} c(\vec{x}) e^{-i\vec{k}\cdot\vec{x}}$. The Kronecker symbol $\delta_{\vec{G}+\vec{G}'+\vec{q}+\vec{q}',0}$ restricts the summation to the terms $\vec{G}' = -\vec{G}$ and $\vec{q}' = -\vec{q}$

$$\begin{aligned} \int d\vec{x}_1 d\vec{x}_2 \Delta\rho(\vec{x}_1)\Delta\rho(\vec{x}_2)C(\vec{x}_1-\vec{x}_2) &= -V\sum_{\vec{G}\vec{q}\alpha\beta} |\rho_0(\vec{G})|^2 \hat{c}((\vec{G}+\vec{q})^2) \times \\ &\times \ \vec{G}_\alpha \vec{G}_\beta \hat{u}_\alpha(\vec{q})\hat{u}_\beta(-\vec{q}). \end{aligned} \tag{3.20}$$

The other term can be easily calculated

$$\begin{aligned} &\int d\vec{x}_1 d\vec{x}_2 \quad \Delta\rho(\vec{x}_1)\Delta\rho(\vec{x}_2)\frac{\rho_l \delta(\vec{x}_1-\vec{x}_2)}{\rho_0(\vec{x})} \\ &= \int d\vec{x}_1 \Delta\rho(\vec{x}_1)\vec{u}(\vec{x}_1)\cdot\nabla\rho_0(\vec{x}_1)\frac{\rho_l}{\rho_0(\vec{x}_1)} \\ &= \int d\vec{x}_1 \Delta\rho(\vec{x}_1)\vec{u}(\vec{x}_1)\cdot\nabla\left[\log\frac{1}{\rho_0(\vec{x}_1)}\right] \\ &= \int d\vec{x}_1 \Delta\rho(\vec{x}_1)\vec{u}(\vec{x}_1)\cdot\nabla_1\int d\vec{x}_2 C(\vec{x}_1-\vec{x}_2)\rho_0(\vec{x}_2). \end{aligned} \tag{3.21}$$

In order to obtain the last line in the equation, it was taken into account that $\rho_0(\vec{x})$ minimizes the free energy (3.12). Using the Fourier expansion of the density and the displacement field and integrating with respect to spatial variables gives

$$\begin{aligned} \int d\vec{x}_1 d\vec{x}_2 \Delta\rho(\vec{x}_1)\Delta\rho(\vec{x}_2)\frac{\rho_l}{\rho_0(\vec{x})}\delta(\vec{x}_1-\vec{x}_2) &= \sum_{\vec{G}\vec{G}'\vec{q}\vec{q}'\alpha\beta} \rho_0(\vec{G})\hat{\rho}_0(\vec{G}')\hat{c}((\vec{G}')^2) \\ &\times \ (iG_\alpha)(iG'_\beta)\hat{u}_\alpha(\vec{q})\hat{u}_\beta(\vec{q}')V\delta_{\vec{G}+\vec{G}'+\vec{q}+\vec{q}'} \\ &= V\sum_{\vec{G}\vec{q}\alpha\beta} |\hat{\rho}_0(\vec{G}')|^2\hat{c}((\vec{G})^2) \\ &\times \ G_\alpha G'_\beta \hat{u}_\alpha(\vec{q})\hat{u}_\beta(\vec{q}'). \end{aligned} \tag{3.22}$$

The harmonic contribution to the free energy is by inserting expressions (3.20) and (3.22) in Eq. (3.18),

$$\frac{\mathcal{F}_{\text{DFT}}^{harm}}{k_BT} = \frac{V}{2}\sum_{\vec{G}\vec{q}\alpha\beta}\hat{\rho}_0(\vec{G})\rho_0(-\vec{G})G_\alpha G_\beta(\hat{c}(\vec{G}^2) - \hat{c}((\vec{q}+\vec{G})^2))u_\alpha(\vec{q})\hat{u}_\beta(-\vec{q}). \tag{3.23}$$

The dynamical matrix is just

$$D_{\alpha\beta} = \frac{V}{2}\sum_{\vec{G}\vec{q}\alpha\beta}\hat{\rho}_0(\vec{G})\rho_0(-\vec{G})G_\alpha G_\beta(\hat{c}(\vec{G}^2) - \hat{c}((\vec{q}+\vec{G})^2))u_\alpha(\vec{q})\hat{u}_\beta(-\vec{q}). \tag{3.24}$$

The fact that we calculated the dynamical matrix does not mean that the model contains phonon dynamics in it, because in the DFT of freezing all the short time scales are integrated out. The simplest way to reintroduce the elastic interactions is to modify the equation of motion to include the second order time derivative term [43]. In this approach, the elastic interactions are mediated through wave modes that propagate on time scales many orders of magnitude slower than atomic vibrations but still much faster than diffusive time scales.

The phonon energy spectrum is determined by the interaction potential which means it is contained in the two particle correlation function. This gives the possibility to use it as input for the theory instead reference liquid two point correlation function a correlation function that reproduces the experimental phonon spectrum [31]. In the next section a similar procedure is applied to the PFC model.

3.3 Distortions energy in the PFC model

The effective energy of the phonon modes can be obtained by expanding up to the second order of the PFC free energy [17],

$$F = \int d\vec{x}\left[\frac{\psi}{2}\left(r + \left(k_0^2 + \nabla^2\right)^2\right)\psi + \frac{\psi^4}{4}\right]. \tag{3.25}$$

The free energy (3.25) is minimized by the density field $\psi_0(\vec{x})$ for the constraint $(1/V_d)\int d\vec{x}\psi(\vec{x}) = \bar{\psi}$. The distorted density is given

$$\psi(\vec{x}, \vec{u}(\vec{x})) = \sum_{\vec{G}} \hat{\psi}_0(\vec{G}) e^{i\vec{G}\cdot(\vec{x}+\vec{u}(\vec{x}))}, \tag{3.26}$$

where $\hat{\psi}_0(\vec{G}) = \int d\vec{x}\psi_0(\vec{x})e^{i\vec{G}\cdot\vec{x}}$. The displacement vectors and the density can be written in terms of the Fourier components as

$$u_\alpha(\vec{x}) = \sum_{\vec{q}} \hat{u}_\alpha(\vec{q}) e^{i\vec{q}\cdot\vec{r}}, \tag{3.27}$$

where $\vec{q}$ is restricted to the first Brillouin zone, while the expression of the equilibrium density, ψ_0, in terms of the Fourier components, is

$$\psi_0 = \sum_{\vec{G}} \hat{\psi}_0(\vec{G}) e^{i\vec{G}\cdot\vec{r}}. \tag{3.28}$$

In order to calculate the harmonic part of the free energy we expand it around the equilibrium density, $\psi_0(\vec{x})$, up to the second order in $\vec{u}(\vec{x})$. Up to the second order in $\vec{u}(\vec{x})$ the distorted density is approximated by

$$\psi = \psi_0 + \psi_1 + \mathcal{O}(u^2), \tag{3.29}$$

where ψ_1 is given by

$$\psi_1(\vec{x}) = \sum_\alpha \left(\frac{\partial\psi_0(\vec{x})}{\partial x_\alpha}\right) u_\alpha(\vec{x}) = i\sum_{\alpha\vec{q}\vec{G}} \hat{\psi}_0(\vec{G}) G_\alpha \hat{u}_\alpha(\vec{q}) e^{i(\vec{G}+\vec{q})\cdot\vec{x}}. \tag{3.30}$$

Inserting (3.3) in the free energy we find the first-order correction to the free energy is

$$F_1 = \int d\vec{x}\psi_1 \left[\mathcal{L}\psi_0 + \psi_0^3\right], \tag{3.31}$$

where $\mathcal{L}(\nabla^2) = r + (k_0^2 + \nabla^2)^2$ is a linear operator with the eigenvalues $\hat{\mathcal{L}}(k^2)$. Because we expand around the equilibrium state, the first order correction to the free energy given by Eq. (3.31) is zero.

The harmonic contribution to the free energy is

$$F^{harm} = \frac{1}{2}\int d\vec{x} \left[\psi_1\mathcal{L}\psi_1 + 3\psi_0^2\psi_1^2\right]. \tag{3.32}$$

The first term in Eq.(3.32) is

$$\begin{aligned}\int d\vec{x}\psi_1\mathcal{L}\psi_1 &= \sum_{\alpha\beta}\sum_{\vec{q}\vec{q}'\vec{G}\vec{G}'}\hat{\psi}_0(\vec{G})\hat{u}_\alpha(\vec{q})G_\alpha\hat{\mathcal{L}}((\vec{q}+\vec{G}')^2)\hat{\psi}_0(\vec{G}')\hat{u}_\beta(\vec{q}')G'_\beta \\ &\times (-1)\int d\vec{x}e^{i(\vec{q}'+\vec{G}'+\vec{q}+\vec{G})\cdot\vec{x}}.\end{aligned} \tag{3.33}$$

The integration with respect to $\vec{x}$ gives $V_d\delta_{\vec{q}+\vec{q}',-\vec{G}-\vec{G}'}$, where V_d is the integration volume. Only for $\vec{q}=-\vec{q}'$ we have a non-zero contribution, which gives $V\delta_{\vec{G},-\vec{G}'}$ and the first term in the harmonic free energy,

$$\int d\vec{x}\psi_1\mathcal{L}\psi_1 = V_d\sum_{\vec{q}}\sum_{\alpha,\beta}\left[\sum_{\vec{G}}\hat{\psi}_0(\vec{G})\hat{\psi}_0(-\vec{G})\hat{\mathcal{L}}(|\vec{q}+\vec{G}|^2)G_\alpha G_\beta\right]\hat{u}_\alpha(\vec{q})u_\beta(-\vec{q}). \tag{3.34}$$

The second term is

$$\int d\vec{x}\psi_1(3\psi_0^2)\psi_1 = \sum_{\alpha,\beta}\int d\vec{x}3\psi_0^2\frac{\partial\psi_0}{\partial x_\alpha}\frac{\partial\psi_0}{\partial x_\beta}u_\alpha u_\beta = \sum_{\alpha,\beta}\int d\vec{x}\frac{\partial(\psi_0^3)}{\partial x_\alpha}\frac{\partial\psi_0}{\partial x_\beta}u_\alpha u_\beta. \tag{3.35}$$

Taking into account that ψ_0 minimizes the free energy, the second term in the harmonic free energy is

$$\int d\vec{x}\psi_1(3\psi_0^2)\psi_1 = -\sum_{\alpha,\beta}\int d\vec{x}\frac{\partial(\hat{\mathcal{L}}(\nabla^2)\psi_0)}{\partial x_\alpha}\frac{\partial\psi_0}{\partial x_\beta}u_\alpha u_\beta. \tag{3.36}$$

This gives

$$\begin{aligned}\int d\vec{x}\psi_1(3\psi_0^2)\psi_1 &= \sum_{\alpha\beta}\sum_{\vec{q}\vec{q}'\vec{G}\vec{G}'}\hat{\psi}_0(\vec{G})\hat{\psi}_0(\vec{G}')\hat{\mathcal{L}}(\vec{G}'^2)G_\alpha G_\beta \\ &\times \hat{u}_\alpha(\vec{q})\hat{u}_\beta(\vec{q}')\int d\vec{x}e^{i(\vec{q}'+\vec{G}'+\vec{q}+\vec{G})\cdot\vec{x}}.\end{aligned} \tag{3.37}$$

The integration with respect to $\vec{x}$ gives $V_d\delta_{\vec{q}+\vec{q}',-\vec{G}-\vec{G}'}$, where V_d is the integration volume. Only for $\vec{q}=-\vec{q}'$ we have non-zero contribution, which gives $V\delta_{\vec{G},-\vec{G}'}$ and the first term in the harmonic free energy is

$$\int d\vec{x}\psi_1(3\psi_0^2)\psi_1 = -\sum_{\alpha\beta}\sum_{\vec{q}\vec{G}}\hat{\psi}_0(\vec{G})G_\alpha G_\beta\hat{\mathcal{L}}(\vec{G}^2)\hat{\psi}_0(-\vec{G})\hat{u}_\alpha(\vec{q})\hat{u}_\beta(-\vec{q}). \tag{3.38}$$

Eqs. (3.34,3.38) added together give us the dynamical matrix,

$$\begin{aligned} D_{\alpha\beta}(\vec{q}) &= \frac{\partial^2 F[\psi]}{\partial \hat{u}_\alpha(\vec{q})\partial \hat{u}_\beta(\vec{q})} \\ &= \sum_{\vec{G}} |\hat{\psi}_0(\vec{G})|^2 G_\alpha G_\beta (\hat{\mathcal{L}}(|\vec{q}+\vec{G}|^2) - \hat{\mathcal{L}}(\vec{G}^2)). \end{aligned} \tag{3.39}$$

The summation in the previous equation is over the relevant reciprocal lattice vectors. In the absence of the pinning potential the summation is done over the reciprocal lattice vectors of magnitude k_0. Close to the first peak of the two point correlation function, this expression is identical with the one obtained in the previous section for the DFT of freezing. This implies that we can obtain results only for $|\vec{q}|$ close to zero. This is enough for calculating the elastic constants and for fitting the parameters of the PFC to match the elastic constants of real materials.

For 1D system the elastic tensor has only one component. Taking into account that all Fourier components except $\hat{\psi}(|\pm k_0|)$ are zero, the dynamical matrix is

$$D_{1D}(q) = |\hat{\psi}_0(k_0)|^2 k_0^2 (2q^4 + 8k_0^2 q^2). \tag{3.40}$$

The bulk modulus for 1D systems can be extracted as

$$\begin{aligned} K &= \frac{1}{2}\frac{\partial^2 D_{1D}(q)}{\partial q^2}|_{q=0} \\ &= 8|\hat{\psi}(k_0)|^2 k_0^4. \end{aligned} \tag{3.41}$$

This expression can be compared to the one derived in Sec. 2.1 taking into account that $A_p^{eq} = 2\hat{\psi}_0(k_0)$, which gives

$$K = 2(A_p^{eq})^2 k_0^4, \tag{3.42}$$

in agreement with the previous calculations done in Sec. 2.1.

In 2D the system forms a hexagonal lattice with six reciprocal lattice vectors of magnitude

k_0

$$\vec{G}_1 = k_0(\sqrt{3}/2\hat{x} + \hat{y}/2); \tag{3.43}$$

$$\vec{G}_2 = -k_0(\sqrt{3}/2\hat{x} + \hat{y}/2); \tag{3.44}$$

$$\vec{G}_3 = k_0\hat{y}; \tag{3.45}$$

$$\vec{G}_4 = -k_0\hat{y}; \tag{3.46}$$

$$\vec{G}_5 = k_0(-\sqrt{3}/2\hat{x} + \hat{y}/2); \tag{3.47}$$

$$\vec{G}_6 = k_0(\sqrt{3}/2\hat{x} - \hat{y}/2). \tag{3.48}$$

The dynamical matrix of the 2D PFC model is

$$D_{xx}(\vec{q}) = 3|\hat{\psi}_0(|\vec{G}| = k_0)|^2 k_0^2(k_0^2(3q_x^2 + q_y^2) + (q_x^2 + q_y^2)^2); \tag{3.49}$$

$$D_{xy}(\vec{q}) = D_{yx}(\vec{q}) = 6|\hat{\psi}_0(|\vec{G}| = k_0)k_0^4|^2 q_x q_y;$$

$$D_{yy}(\vec{q}) = 3|\hat{\psi}_0(|\vec{G}| = k_0)|^2 k_0^2(k_0^2(q_x^2 + 3q_y^2) + (q_x^2 + q_y^2)).$$

The elastic constant tensor is obtained from the dynamical matrix through the relation [13]

$$D_{\alpha\beta}(\vec{q}) = \sum_{\mu\nu} K_{\alpha\mu\beta\nu} q_\mu q_\nu, \tag{3.50}$$

where

$$K_{\alpha\mu\beta\nu} = \frac{1}{2}\frac{\partial^2 D_{\alpha\beta}}{\partial q_\mu \partial q_\nu}. \tag{3.51}$$

For the hexagonal lattice there are three independent elastic constants [4]

$$C_{11} = K_{xxxx} = K_{yyyy}; \tag{3.52}$$

$$C_{12} = K_{xxyy} = K_{yyxx};$$

$$C_{44} = K_{xyxy} = K_{yxyx}.$$

Substituting Eq. (3.50) in Eq. (3.52) and taking into account that $4\hat{\psi}(|\vec{G}| = k_0) = A_t^{eq}$ we obtain

$$C_{11} = \frac{9(A_t^{eq})^2}{16}k_0^4; \tag{3.53}$$

$$C_{12} = \frac{3(A_t^{eq})^2}{16}k_0^4;$$

$$C_{44} = \frac{3(A_t^{eq})^2}{16}k_0^4,$$

in agreement with the calculations presented in Sec. 2.2.

We now turn the attention to 3D systems. In 3D, the configuration that minimizes the free energy (2.3) forms a BCC lattice with 12 reciprocal vectors that satisfy the condition $|\vec{G}| = k_0$ [4]

$$\begin{aligned} &\tfrac{2\pi}{a\sqrt{2}} \quad (\pm\hat{y} \pm \hat{z}) \\ &\tfrac{2\pi}{a\sqrt{2}} \quad (\pm\hat{x} \pm \hat{z}) \\ &\tfrac{2\pi}{a\sqrt{2}} \quad (\pm\hat{x} \pm \hat{y}), \end{aligned} \tag{3.54}$$

where all choices of sign are independent. The dynamical matrix of the BCC crystal is

$$\begin{aligned} D_{xx}(\vec{q}) &= 4|\hat{\psi}_0(|\vec{G}| = k_0)|^2 k_0^2 (q_x^2 + q_y^2 + q_z^2)(k_0^2 + q_x^2 + q_y^2 + q_z^2); \\ D_{yy}(\vec{q}) &= 4|\hat{\psi}_0(|\vec{G}| = k_0)|^2 k_0^2 (q_x^2 + q_y^2 + q_z^2)(k_0^2 + q_x^2 + q_y^2 + q_z^2); \\ D_{zz}(\vec{q}) &= 4|\hat{\psi}_0(|\vec{G}| = k_0)|^2 k_0^2 (q_x^2 + q_y^2 + q_z^2)(k_0^2 + q_x^2 + q_y^2 + q_z^2); \\ D_{xy}(\vec{q}) &= D_{xy}(\vec{q}) = 8|\hat{\psi}_0(|\vec{G}| = k_0)|^2 k_0^4 q_x q_y; \\ D_{xz}(\vec{q}) &= D_{xz}(\vec{q}) = 8|\hat{\psi}_0(|\vec{G}| = k_0)|^2 k_0^4 q_y q_z; \\ D_{yz}(\vec{q}) &= D_{zy}(\vec{q}) = 8|\hat{\psi}_0(|\vec{G}| = k_0)|^2 k_0^4 q_z q_x. \end{aligned} \tag{3.55}$$

For cubic symmetry there are three independent elastic constants [4]

$$\begin{aligned} C_{11} &= \frac{A_{BCC}^2}{2} k_0^4 \\ C_{12} &= \frac{A_{BCC}^2}{4} k_0^4 \\ C_{44} &= \frac{A_{BCC}^2}{4} k_0^4 \end{aligned} \tag{3.56}$$

In last expression we took into account that $4\hat{\psi}(|\vec{G}| = k_0) = A_{BCC}^{eq}$. Using the expression obtained for the elastic moduli the parameters can be fit to recreate the elastic properties of real materials and study. The expression (3.39) is a general expression valid for all dimensions and all symmetries and it can be used also if the correlation function approximation contains additional peaks. This expression can be used also for calculating the elastic constants of metastable states or the commensurate phases that minimize the free energy in the presence of a periodic pinning potential.

In the next section the PFC model is extended to include the effect of external potential of different lattice constant and symmetry of the original PFC, leading to competition between the intrinsic ordering of the system and the pinning potential.

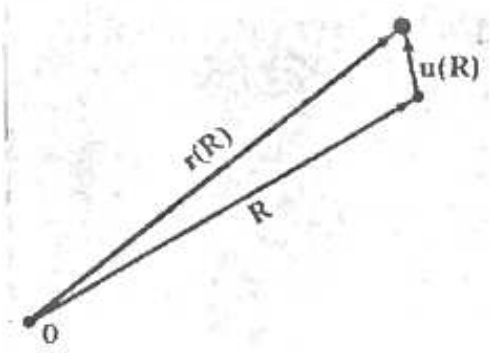

Figure 3.1: The relation between the Bravais lattice vectors $\vec{R}$, instantaneous position $\vec{r}(\vec{R})$ of the particle that oscillates a round $\vec{R}$ and the displacement, $\vec{u}(\vec{R}) = \vec{r}(\vec{R}) - \vec{R}$, according to Ref. [4].

4 The PFC model in external potential

In this chapter we present our analysis of the effect of an external pinning potential. This is relevant to many systems in nature that possess two or more competing length scales. Such systems may exhibit both commensurate and incommensurate phases [51, 5] characterized by differences in the spatial ordering of the system. Important examples include spin density waves [53, 18], charge density waves [47], vortex lattices in superconducting films with pinning centers [30] and weakly adsorbed monolayers [3, 48] on a substrate. The emerging structures are characterized by an order parameter (*e.g.* charge, spin or particle density) that is modulated in space with a given wave vector q usually incommensurate with the underlying lattice. In particular, for 2D adsorbate systems, there is competition between the commensurate state, which is favored by a strong periodic pinning potential and the cost of the elastic energy depending on the mismatch between the intrinsic lattice constant a of the overlayer, and the period a_s of the pinning potential. The effect of a substrate can be easily taken into account by introducing a linear coupling term in the free energy, $\int d\vec{x} V(\vec{x})\psi(\vec{x})$, as shown in Refs. [10, 11, 12]. Two types of external potentials were studied: a periodic potential and randomly distributed defects.

In the first part of this section the effect of the simple periodic potential is presented. For the 1D case the periodic potential reduces to $V_0 \cos(k_s x)$, while for 2D a potential with square symmetry was considered. A potential with square symmetry is usually found when a layer is adsorbed on a 100 or 110 face of a BCC crystal. The strength of the coupling is characterized by the pinning strength V_0 and the relative mismatch, δ_{m}, between the periodicity of the potential k_s and k_0. The effect of the periodic potential was studied in the absence of of thermal fluctuations for both 1D and 2D case, while for the 2D systems also the effect of thermal fluctuations was investigated. We studied the effect of the thermal fluctuations using MC simulations with a standard Metropolis algorithm in the grand-canonical ensemble following Ref. [29].

In the end of the chapter, the effect of randomly distributed defects is presented for 2D systems in the absence of thermal fluctuations. In this case the effective potential can be written as a sum of randomly distributed attractive centers. The configuration of the system will depend on the pinning strength V_0, the density of centers and the ratio between the width of the centers and the lattice constant of the undisturbed hexagonal lattice.

4.1 Periodic potential at zero temperature

In this section we will discuss the effect of periodic pinning potential in the absence of thermal fluctuations for the 1D and 2D systems. The parameters $(\bar{\psi}, r)$ are set so that the system is in a solid phase, $(\bar{\psi} = -1/4, r = -1/4)$. The effect of a substrate is introduced using a linear coupling term $\int d\vec{x} V(\vec{x})\psi(\vec{x})$ in the free energy given by (2.3)

$$F = \frac{1}{V_d}\int d\vec{x}\left[\frac{\psi}{2}\left(r + \left(k_0^2 + \nabla^2\right)^2\right)\psi + \frac{\psi^4}{4} + V(\vec{x})\psi(\vec{x})\right]. \tag{4.1}$$

The periodic pinning potentials are characterized by the coupling amplitude V_0 and the lattice mismatch

$$\delta_{\mathrm{m}} = \frac{k_0 - k_s}{k_0}, \tag{4.2}$$

where $k_s = 2\pi/a_s$ and a_s is the distance between two minima of the potential. It is expected that in the limit $V_0 \to 0$ or a relatively small coupling the system will be in an I state. In the opposite limit, of large V_0, the pinning potential will dominate and the system will be in a state commensurate with the external potential, *i.e.* the ratio between the relevant reciprocal lattice of the system and the reciprocal vectors of the pinning potential is a rational number.

Numerically, in the absence of the fluctuations, the equilibrium states are obtained by solving the equation of motion:

$$\frac{\partial\psi}{\partial t} = \nabla^2\frac{\delta F[\psi]}{\delta\psi} = \nabla^2\left(r + (k_0^2 + \nabla)^2)\psi + \psi^4 + V\right). \tag{4.3}$$

The limit $t \to \infty$ corresponds to equilibrium ($\delta F[\psi]/\delta\psi = $ constant). Eq. (4.3) was integrated explicitly using finite difference on a uniform grids (1D and 2D) with discretization $dx = dy = \pi/4$ and time step $dt = 0.005$. For one 1D systems the size of the grid was varied from $16384dx$ to $65536dx$, but no significant difference was found in the phase diagrams between different sizes. The energy of the triangular phase in the absence of an external pinning potential has an oscillating dependence with respect to the grid size $l_x \times l_x dx^2$ of the order of 5% of the energy because a triangular phase can not be accommodated on a square grid. Despite this for the case of periodic potentials there was no difference in results when the system size was varied from $256 \times 256dx^2$ to $1024 \times 1024dx^2$[10]. The results presented in Sec 4.1 were obtained using a system size of $65536dx$ for the 1D case and $1024 \times 1024dx^2$ for the 2D case. Even if the size of the system does not affect the significantly the positions of the boundary between different phases (less than 2%), it is important for the study of I phases close to transitions. The laplacians are evaluated in 1D using a central difference, while for the 2D the 'spherical laplacian' is used [17, 44]. Fully periodic boundary conditions have been used, which limits the value of k_s that can be used to the ones that satisfy $k_s = 2\pi n/(l_x dx)$, with n integer. Because there are no fluctuations, the system can evolve towards a local minimum or the global minimum depending on the initial configuration. In order to find the global minimum different initial configurations where used and after equilibration the one with the lowest energy is selected. In the case of periodic potentials we have studied the influence of the potential also analytically. In the analytical approach the equilibrium state was found using a trial function (2.7), where the relevant terms correspond to commensurate and incommensurate states. After the integration with respect to spatial variables, the free energy corresponding to the trial function was minimized with respect to the amplitudes $a_{\vec{G}}$.

4.1.1 One dimensional system

First we present the results regarding the effect of a periodic pinning potential for a 1D system following Ref. [12]. The external pinning potential is

$$V(x) = V_0 \cos(k_s x). \tag{4.4}$$

For $V_0 = 0$ the state that minimizes the free energy is given by (2.8), while in the large V_0 limit the system is going to be an state which is an exact match of the pinning potential (4.4). The trial function used for the analytical calculation is

$$\psi(x) = A_p \cos(k_p x) + A_v \cos(q_s x) + A_i \cos((2k_p - k_s)x). \tag{4.5}$$

This approximation of the density field contains a combination of the terms corresponding to the free lattice $(A_p \cos(x))$ and pinning potential $(A_v \cos(k_s x))$ plus an extra term $(A_i \cos((2 - k_s)x))$ which appears due to distortion of the lattice. After inserting this expression in (4.1) and integrating over space, the free energy is found to be

$$\begin{aligned} F_{1D}^{\text{pin}}/L &= \frac{1}{4}A_i^2(r + 3\bar{\psi}^2 + (k_0^2 - (2k_p - k_s)^2)^2) + \frac{3}{32}A_i^4 \\ &+ \frac{1}{4}A_v^2(r + 3\bar{\psi}^2 + (k_0^2 - k_s^2)^2) + \frac{3}{32}A_v^4 \\ &+ \frac{1}{2}V_0 A_v + \frac{3}{8}(A_p^2 A_v A_i + A_v^2 A_i^2 + A_p^2 A_v^2 + A_p^2 A_i^2) + F_p/L, \end{aligned} \tag{4.6}$$

where F_p/L is the energy of the 1D free lattice given by (2.9) and $k_p = k_0$. The amplitudes A_p, A_v, A_i are found by minimizing Eq. (4.6). All three amplitudes depend on the lattice mismatch and pinning amplitude. For a fixed δ_m and large enough V_0, $A_p = A_i = 0$ and the system is in C phase, while for small values of the pinning amplitudes the system is found in I phase, $A_p \neq 0$ and $A_i \neq 0$. The transition point is defined as the values of (δ_{m}, V_0) at which the amplitude A_p vanishes. Examples of I phases are shown in Figs. 4.1(a) (for $V_0 = 0$) and Fig. 4.2(a) ($V_0 = 0.021197, \delta_m = 0.125$), while in Fig. 4.3(a) a C phase is shown for $(\delta_{\text{m}} = 0.125, V_0 = 0.04608)$. The corresponding structure factor, $S(k) = \hat{\psi}(k)\hat{\psi}(-k)$, where $\hat{\psi}(k) = (1/L)\int dx \psi(x) \exp(ikx)$ and the density field $\psi(x)$ is obtained numerically to minimize the free energy (4.1), for each case is also presented (Figs. 4.1(b),4.2(b) and 4.3(b)).

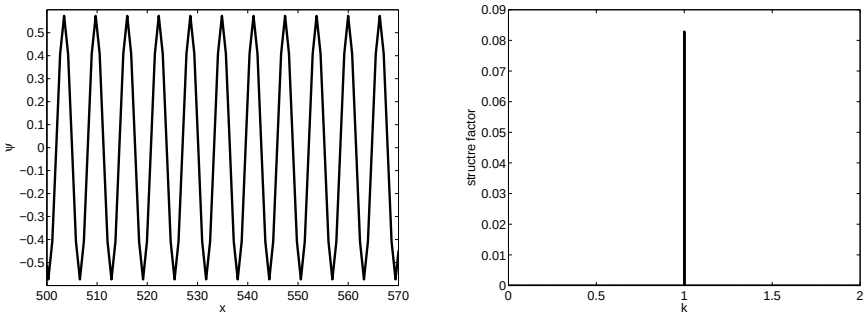

(a) (b)

Figure 4.1: (a) Density configuration and (b) the structure factor for $\delta_m = 0.125$ and $V_0 = 0.00$.

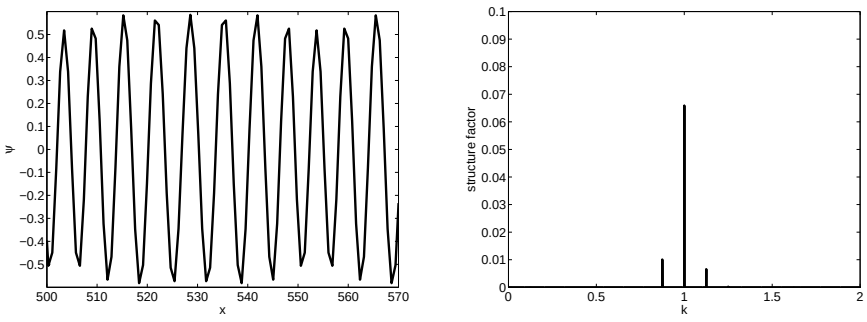

(a) (b)

Figure 4.2: (a) Density configuration and (b) the structure factor for $\delta_m = 0.125$ and $V_0 = 0.021197$.

Within the range of parameters used for the 1D system we found only one C phase, which was an exact match of the pinning potential (the lattice constant of the system is equal to the lattice constant of the substrate). Numerically, the order parameter A_p can be calculated from the Fourier transform of the density field, $A_p = \hat{\psi}(k_p) + \hat{\psi}(-k_p)$. Fig. 4.4 shows the phase diagram calculated numerically and analytically.

The dependence of the A_p, both in analytical and numerical calculations, suggests a dis-

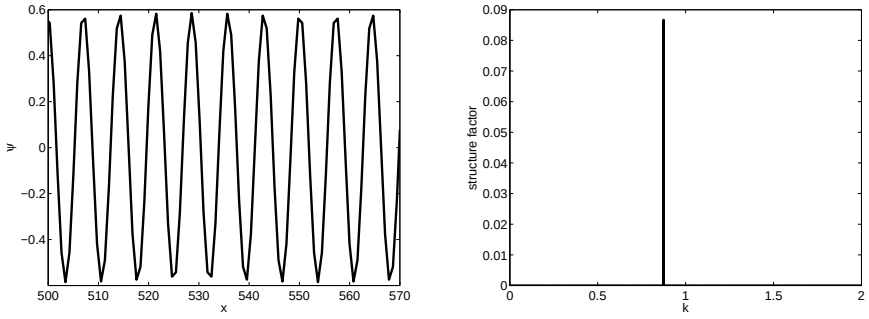

(a) (b)

Figure 4.3: (a) Density configuration and (b) the structure factor for $\delta_{\rm m} = 0.125$ and $V_0 = 0.04608$.

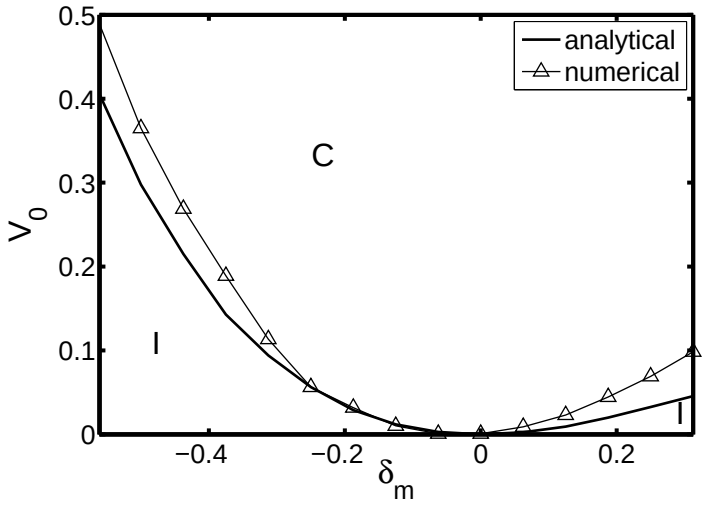

Figure 4.4: Phase boundary for the 1D system, calculated numerically (continuous line) and analytically (dashed line). Commensurate regions are denoted by C, while the incommensurate regions by I.

continuous I-C transition for $-0.375 \leq \delta_{\rm m} \leq 0.6875$ (Fig. 4.5(a)), while for $\delta_{\rm m} < -0.375$ the type of transition changes to a continuous one (Fig. 4.5(b)).

The energy hysteresis shows that in the range of mismatches, $-0.375 \leq \delta_{\rm m} \leq 0.6875$,

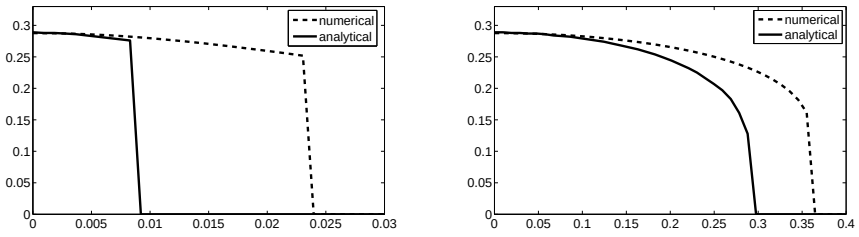

(a) $\delta_{\mathrm{m}} = 0.125$ (b) $\delta_{\mathrm{m}} = -0.50$

Figure 4.5: Dependence of A_p with respect to pinning strength calculated numerically (dashed line) and analytically (continuous line) for (a) $\delta_{\mathrm{m}} = 0.125$ and (b) $\delta_{\mathrm{m}} = -0.50$.

for a given value of V_0 there is a local minimum corresponding to C and a local minimum corresponding I separated by an energy barrier. Depending on the initial configuration, the system will evolve towards one or the other minima. When V_0 is at its critical value, the C state has a lower energy than the I state (Fig. 4.6(a)) suggesting a discontinuous I-C phase transition. For $\delta_{\mathrm{m}} < -0.375$ there is no hysteresis in the energy (Fig. 4.6(b)), suggesting a continuous transition.

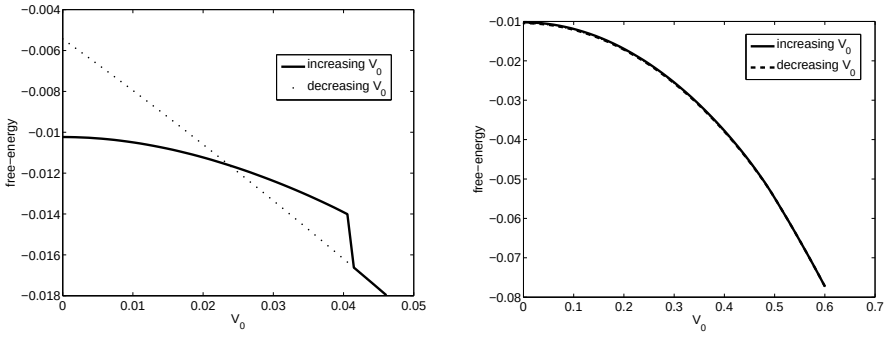

(a) $\delta_{\mathrm{m}} = 0.125$ (b) $\delta_{\mathrm{m}} = -0.50$

Figure 4.6: Dependence of the free energy on the pinning strength calculated numerically for increasing pinning strength (continuous line) and decreasing pinning strength (dotted line) for (a) $\delta_{\mathrm{m}} = 0.125$ and (b) $\delta_{\mathrm{m}} = -0.50$.

4.1.2 Two dimensional case

The effect of an external potential was also studied for 2D systems in Refs. [10, 11]. The interaction between the adsorbate and the substrate was chosen to be

$$V(\vec{x}) = V_0(\cos(k_s x) + \cos(k_s y)). \tag{4.7}$$

For $V_0 = 0$ the ground state has a perfect triangular symmetry. With increasing amplitude of the pinning potential the configurations become spatially distorted and eventually the system undergoes a transition to a square symmetry C phase. Because the pinning potential has a different symmetry from the free lattice and there are no thermal fluctuations the transition from a I phase to a C phase is of the first order.

Numerically, the ground state is found by solving the equation of motion (4.3). Several different initial configurations (hexagonal and C phases) were used. The equilibrium state for each V_0 and $\delta_{\rm m}$ is the one with the lowest energy. Several states were found to minimize the free energy. For small values of the pinning strength the system is in a hexagonal incommensurate phase for all mismatches (Fig. 4.7(a)). If the pinning strength is large enough, the system will be in one of the commensurate phases. The (1×1) phase is an exact match with the pinning potential (Fig. 4.7(b)).

In addition to the (1×1) phase, higher commensurate phases exist when the relevant reciprocal lattice vectors are close to k_0. One these phases is the $\mathrm{c}(2 \times 2)$ phase in which every second site of the lattice of the pinning potential is occupied [51] (Fig. 4.7(d)). The relevant reciprocal vectors have a magnitude of $k_s/\sqrt{2}$. This state is favored for mismatch values close to $1 - \sqrt{2}$ (Fig 4.9(a)). Another higher commensurate phase is the (2×1) phase which is generated by a translation of the basis with the reciprocal lattice vectors of the a $\mathrm{c}(2 \times 1)$ lattice [51] (Fig. 4.7(c)). The structure factor, $S(\vec{k}) = \hat{\psi}(\vec{k})\hat{\psi}(-\vec{k})$ ($\hat{\psi}(\vec{k}) = (1/S)\int d\vec{x}\psi(\vec{x})e^{i\vec{k}\cdot\vec{x}}$) of this phase contains a set of peaks corresponding to the (1×1) phase and a set of peaks located between the first and second order peaks of the (1×1) phase. The magnitude of the reciprocal vector which gives the position of this set

of peaks is $k_s\sqrt{5}/2$, suggesting that this phase is favored to exist when the mismatch is close to 0.1 (Fig 4.9(a)). The $(2\sqrt{2}\times\sqrt{2})$ phase is similar to the (2×1) phase. The lattice is generated by a translation of the basis with vectors which are rotated 45° with respect to the pinning potential and the magnitudes of the vectors are $2\sqrt{2}b$ and $\sqrt{2}b$. The structure factor contains a set of peaks corresponding to the $\mathrm{c}(2\times2)$ phase, while the position of the additional peaks is given by a vectors with magnitude $k_s\sqrt{10}/4$. This phase is favored for mismatch values close to -0.27 (Fig 4.9(a)).

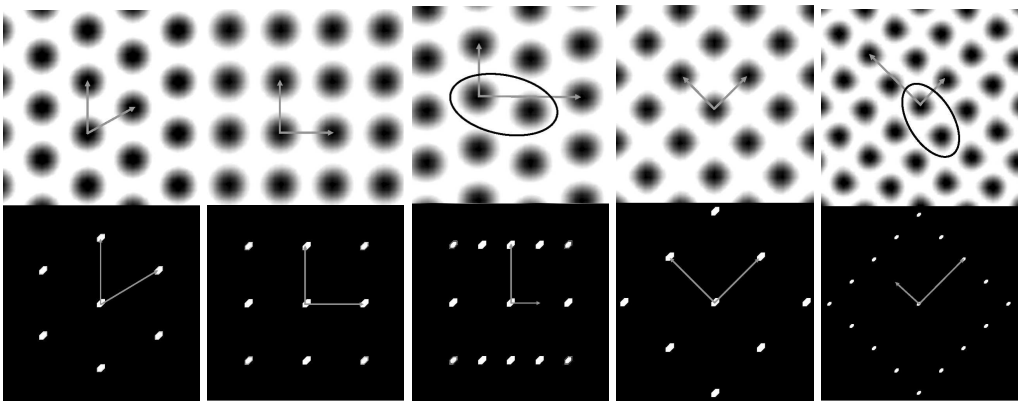

(a) (b) (c) (d) (e)

Figure 4.7: The phases that minimize the free energy: (a) hexagonal, (b) square (1×1), (c) square (2×1), (d) square $\mathrm{c}(2\times2)$, and (e) square $2\sqrt{2}\times\sqrt{2}$. The upper panels represent the density plotted in a gray colormap and the corresponding lattice vectors, while the lower panels the structure factors and the relevant reciprocal lattice vectors. The black contours in Figs. 4.7(c) and 4.7(e) show the bases which generate the (2×1) and $(2\sqrt{2}\times\sqrt{2})$ lattices.

In addition to the ordered phases mentioned above, for the range of system sizes studied here, we found that a number of more complex phases, appear in the range $\delta_{\mathrm{m}}\in[0.2,0]$. These phases are crossover phases between the (2×1) and $\mathrm{c}(2\times1)$ or (2×1) and $2\sqrt{2}\times\sqrt{2}$ structures. Some typical structures are shown in Fig. 4.8.

The transitions between the different phases were found by investigating the positions and the heights of the peaks in the structure factor. A complete diagram is shown in Fig.

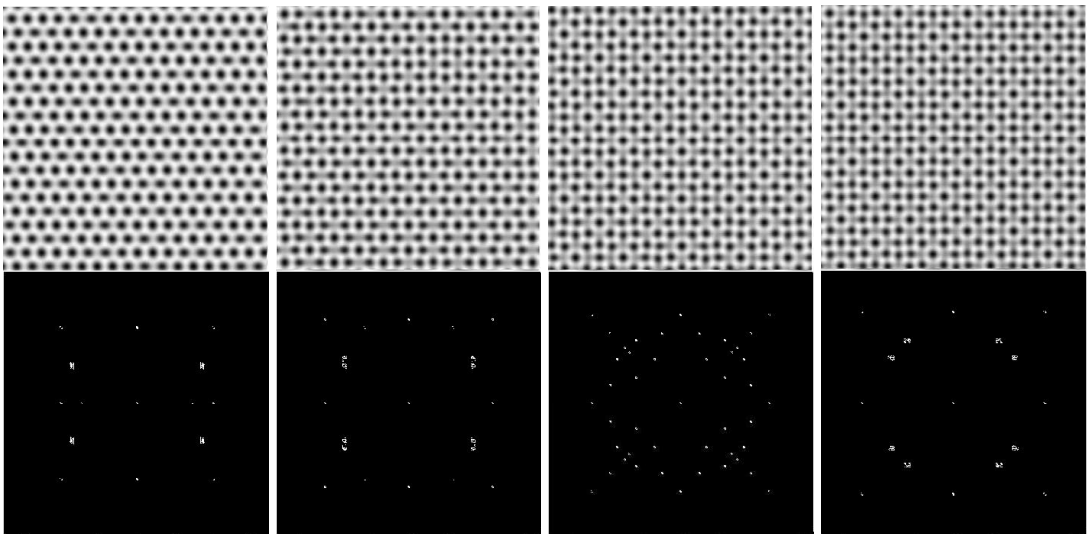

(a) (b) (c) (d)

Figure 4.8: Examples of more complex phases: (a) $\delta_{\rm m} = -0.0156, V_0 = 0.02516$; (b) $\delta_{\rm m} = -0.1250, V_0 = 0.040$; (c) $\delta_{\rm m} = -0.1875, V_0 = 0.0624$ and (d) $\delta_{\rm m} = -0.2188, V_0 = 0.0798$. The upper panels show the density plotted in a gray colormap, while the lower panels the corresponding structure factors.

4.9(a) for $-0.6 < \delta_{\rm m} < 0.3$.

In the analytical method we consider the density to be a sum of hexagonal and square modes. The trial density has the form

$$\begin{aligned} \psi(\vec{x}) &= A_t(\cos(x\sqrt{3}/2)\cos(y/2) - \frac{1}{2}\cos(y)) + A_{s1}(\cos(k_s x) + \cos(k_s y)) \\ &+ A_{s2}\cos(k_s x)\cos(k_s y) + A_c\cos(\frac{k_s}{2}x)\cos(\frac{k_s}{2}x) + \bar{\psi}. \end{aligned} \tag{4.8}$$

The free energy corresponding to this density is

$$\begin{aligned} F_{2D}^{\rm pin}/S &= F_t/S + \frac{3}{8}A_{s1}A_{s2}A_c^2 + \frac{3}{2}A_{s1}^2A_{s2}\bar{\psi} + \frac{3}{4}A_{s1}A_c^2\bar{\psi} + \frac{9}{16}A_{s1}^2A_{s2}^2 \\ &+ \frac{9}{64}At^2(4A_{s1}^2 + A_{s2}^2 + A_c^2) + \frac{3}{32}A_c^2(A_{s2}^2 + 6A_{s1}^2 + 2A_{s2}\bar{\psi}) \\ &+ \frac{1}{8}A_c^2(3\bar{\psi}^2 + r + (k_0^2 - (1/2)k_s^2)^2) + \frac{1}{2}A_{s1}^2(r + 3\bar{\psi}^2 + (k_0^2 - k_s^2)^2) \\ &+ \frac{1}{8}A_{s2}^2(3\bar{\psi}^2 + r + (k_0^2 - (2)k_s^2)^2) + \frac{9}{16}A_{s1}^4 + \frac{9}{256}A_c^4 + \frac{9}{256}A_{s2}^4 + A_{s1}V_0, \end{aligned} \tag{4.9}$$

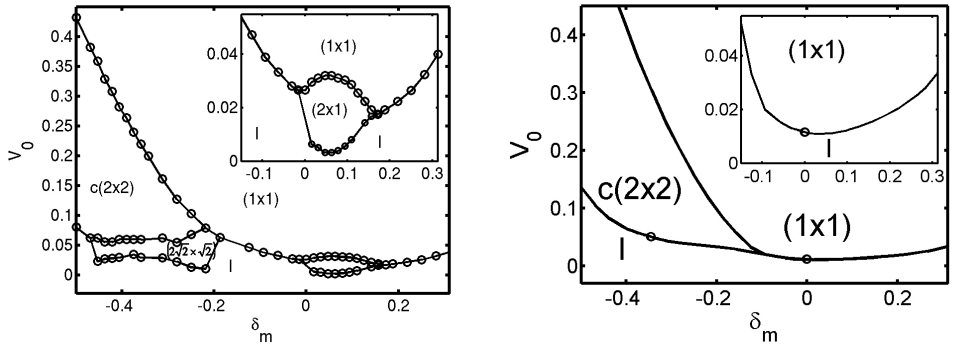

Figure 4.9: The phase diagram in terms of pinning strength (V_0) and mismatch $\delta_{\rm m}$ calculated (a) numerically and (b) analytically. The insets show the phase diagram close to $\delta_{\rm m} = 0$. The circles in (b) mark the values for which the approximation for the density given by Eq. (4.8) breaks down.

where F_t is the free energy of the triangular phase given by Eq. (2.16). The amplitudes A_t, A_{s1}, A_{s2}, A_c are found by minimizing the $F_{2D}^{\rm pin}$. In the density expansion (4.8) the term $A_c \cos(\frac{k_s}{2}x)\cos(\frac{k_s}{2}x)$ corresponds to the c(2×2) phase and the amplitude A_c is non-zero only for $\delta_{\rm m} < -0.25$. The amplitude A_c is a good order parameter to study the c$(2\times 2) \rightarrow (1\times 1)$ phase transition. Both numerically and analytically it was found that, for a fix mismatch, A_c goes to zero continuously when the pinning strength is increased which suggests that c$(2\times 2) \rightarrow (1\times 1)$ transition is continuous. The phase diagram obtained with the mode expansion (4.8) is shown in Fig. 4.9(b). Both numerically and analytically, the transition from the I phase to C phase occurs when $A_t = 0$. Numerically the amplitude A_t is calculated from the Fourier transform of the density field that minimizes the free energy

$$A_t = 4\sum_{\rm hex} \hat{\psi}(\vec{G})/6,$$

where $\sum_{\rm hex}$ indicates that the summation is performed only over the smallest reciprocal lattice vectors of the hexagonal phase and $\hat{\psi}(\vec{k}) = (1/S)\int d\vec{x}\exp(i\vec{k}\cdot\vec{x})\psi(\vec{x})$. The dependence of A_t with respect to V_0, when $\delta_{\rm m}$ is fixed, suggests a discontinuous transition from an I phase to a C phase, while we expect the phase transitions between any two

different C phases to be continuous.

4.2 Thermal fluctuations and phase diagrams of the PFC model with periodic pinning potential

Next, we have studied the effect of thermal fluctuations for the 2D systems in the presence of the square periodic pinning potential. The MC simulations were performed in the grand-canonical ensemble. We modified the free energy expression (4.1) to include an additional linear term to the free energy containing the chemical potential μ, which controls the average value of $\psi(\vec{x})$. This leads to a model *mean field* free-energy functional

$$F_\mu = F_0 \int d\vec{x}\{\frac{1}{2}\psi[r + (k_0^2 + \nabla^2)^2]\psi + \frac{\psi^4}{4} + V\psi - \mu\psi\}, \tag{4.10}$$

where $F_0 = \lambda^2 q^{8-d}/u$. This modification allows the use of the MC algorithm with non-conserved dynamics as described in Sec. 4.2.1, which is more efficient for equilibrium simulations.

In the absence of the pinning potential, $V(\vec{x}) = 0$, the free energy of Eq. (4.10) can be minimized by a configuration of the field $\psi(\vec{x})$ forming a hexagonal pattern of peaks with wavevector of magnitude k_0, when the values of the parameters r and μ are chosen appropriately. This structure of peaks can be regarded as a crystalline system and the free energy functional of Eq. (4.10) can then be used to describe both elastic and plastic properties of such a lattice system within a mean field description [35, 17, 34] for temperatures T below the mean field melting temperature T_m by setting the parameter $r \propto T - T_m$. However, the free energy of Eq. (4.10) does not provide all the information on the system at finite temperatures and specially does not take into account strong thermal fluctuations which may lead to the melting of the hexagonal pattern.

To go beyond mean the field theory and take thermal fluctuations into account, we followed the usual procedure of introducing a coarse-grained effective Hamiltonian [13, 24]

where the energy for a particular configuration of the order parameter is given by the corresponding mean field free-energy functional. Instead of considering only the minimum energy, this procedure allows for excitations according to a statistical weight provided by the free energy functional. In the present case we take as the effective Hamiltonian $H[\psi] \equiv F_\mu[\psi]$ with the corresponding partition function

$$Z = \sum_{\{\psi(\vec{x})\}} e^{-H[\psi]/k_B T}, \tag{4.11}$$

where T is the temperature and the summation (functional integration) is taken over all configurations of $\psi(\vec{x})$. Physical quantities are defined in the usual way as thermal averages over ψ configurations [13, 24]. The parameter r contained in $H[\psi]$ was considered to be a temperature-independent constant for the region below the mean field transition temperature T_m in the absence of the pinning potential.

As in the previous section, we consider a pinning potential $V(x, y)$ with square symmetry

$$V(x, y) = V_0[\cos(k_s x) + \cos(k_s y)], \tag{4.12}$$

with $k_s = 2\pi/a_s$.

4.2.1 Monte Carlo simulations

The free energy associated with the partition function of Eq. (4.11), which now takes thermal fluctuations into account, cannot be obtained directly without approximations. In order to obtain the equilibration configurations and average quantities it is necessary to perform numerical simulations and for this purpose we used the MC method. Thermal averages over configurations of $\psi(x, y)$ were performed using MC simulations on a discrete version of the effective Hamiltonian $H[\psi]$. The field $\psi(x, y)$ and pinning potential $V(x, y)$ were defined on a square space grid, $x = idx$, $y = jdy$ (i, j integers), with grid size $Ldx \times Ldx$, grid spacing $dx = dy$ and with periodic boundary conditions. The

laplacians in Eq. (4.10) were approximated by a simple discretization scheme

$$\frac{\partial^2}{\partial x^2} f_{i,j} = \frac{f_{i+1,j} + f_{i-1,j} - 2f_{i,j}}{(\Delta x)^2}. \tag{4.13}$$

We used the standard Metropolis algorithm for simulations at a given temperature. At each grid site (i, j), we attempt to change $\psi_{i,j}$ by a small amount $\Delta\psi$ with probability $\min(1, e^{-\Delta H/k_B T})$, using the Metropolis scheme, where ΔH is the resulting change in the configurational energy. In our simulations, L was typically ranging from $64dx$ to $224dx$, with the grid spacing $dx = \pi/4$, and $(4 - 2) \times 10^6$ MC passes for equilibration and equal number of passes for thermal averages. Because of the periodic boundary conditions, the length of the system L dx has to be a multiple of the lattice constant of the pinning potential, $2\pi/k_s$. This condition imposes a restriction on the values of k_s when calculations are performed for fixed L and dx. Thus, to be able to change k_s continuously near a commensurate phase while still keeping the same system size L, we choose a variable grid spacing $dx = (k_s^0/k_s)(\pi/4)$, where k_s^0 was fixed such that $L\pi/4 = n(2\pi/k_s^0)$ (n is an integer). The parameters r and μ were set to $r = -1/4$ and $\mu = -0.1875$, corresponding to the hexagonal crystalline region in the original PFC model without pinning [35, 17]. The temperature T is measured in units of $F_0 k_B^{-1}$.

Near the phase transitions, where long equilibration times are required, we used the exchange MC method (parallel tempering) [28, 39]. This method is known to reduce significantly the critical slowing down near phase transitions. Recently, it has been used to study glassy incommensurate vortex lattices in 2D superconducting arrays [25]. In this method, many replicas of the system with different temperatures T_i in a range above and below the critical temperature are simulated simultaneously and the corresponding configurations are allowed to be exchanged with a probability distribution satisfying detailed balance. The exchange process allows the configurations of the system to explore the temperature space, being cooled down and warmed up, and the system can in principle escape more easily from metastable minima at lower temperatures. Without the replica exchange step, the method reduces to conventional MC simulations performed at different temperatures. The method was implemented by performing MC simulations as described

above for each replica at different temperatures, simultaneously and independently, for a few MC passes. Then exchange of pairs of replica configurations at temperatures T_i and T_j and energies E_i and E_j is attempted with probability $\min(1, \exp(-\Delta))$, where $\Delta = (1/T_i - 1/T_j)(E_j - E_i)$, using the Metropolis scheme. We typically used 10^6 MC passes for equilibration with up to 30 replicas and an equal number of MC passes for calculations of average quantities.

4.2.2 Ground-state phase diagram in the grand canonical ensemble

We obtained the ground state ordered structures by simulations of the dissipative dynamical equations for the phase field $\psi(\vec{x})$, as in the previous work [10, 11]. We chose this method because at very low temperatures, the MC method (Sec. 4.2.1) appeared to be computationally less efficient due to the low acceptance rate for MC moves. The dissipative dynamics should evolve the system to the lower-energy state for arbitrary initial conditions. Therefore the determination of the final configurations is equivalent to finding the ground state for the effective Hamiltonian in Eq. (4.11), since $H[\psi] \equiv F_\mu[\psi]$. For the free-energy functional of Eq. (4.10) with non-conserved field the dynamical equations are

$$\frac{\delta\psi}{\delta t} = -\frac{\delta F_\mu}{\delta\psi}. \tag{4.14}$$

The ground-state phase diagram was obtained, numerically, by finding the final configurations where $\delta\psi/\delta t = 0$ starting from different initial configurations, for different misfits δ_m and amplitudes of the pinning potential V_0. Typically, we start with a hexagonal structure, which is the minimum energy state in the absence of the periodic potential ($V_0 = 0$) and then slowly increase V_0 to the its final value for fixed $\delta_{\rm m}$. The calculations are then repeated for different initial conditions. The ground state is the final configuration corresponding to the lowest energy. The equation of motion (4.14) was solved on a uniform square grid of size 128×128 with discretization $dx = \pi/4$. Three low-order commensurate structures were obtained as shown in Fig. 4.10: a (1×1) commensurate (C) phase, where the peaks of $\psi(\vec{x})$ coincide with the pinning potential minima; a $c(2 \times 2)$ C

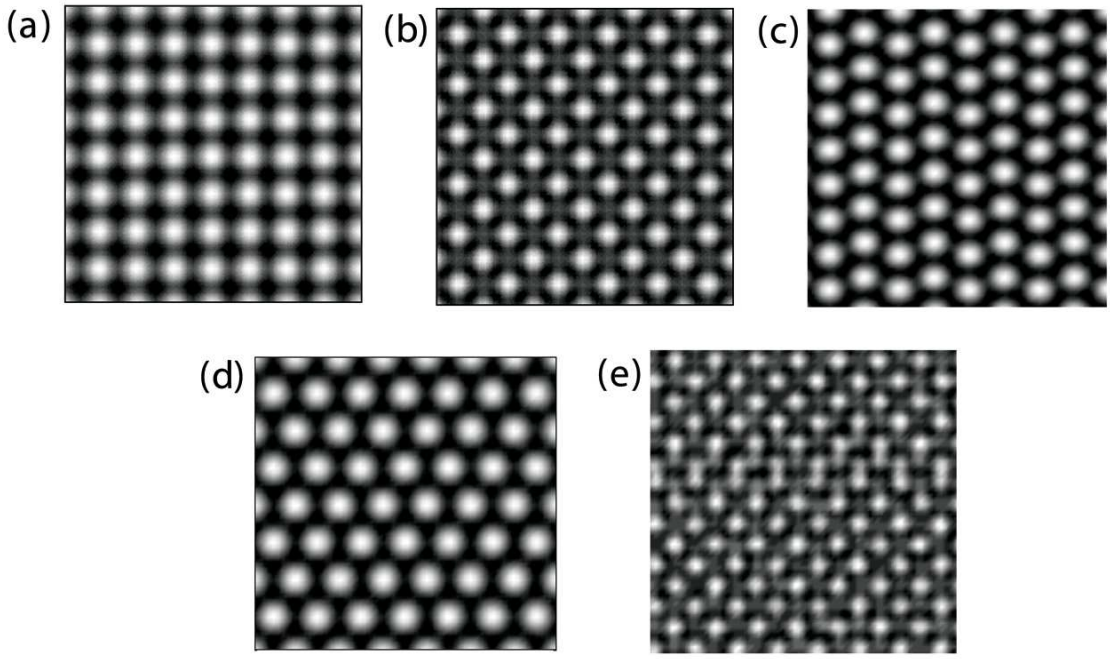

Figure 4.10: Density plot of the phase field $\psi(\vec{x})$ showing commensurate (C) and incommensurate (I) structures in the ground state, depending on the amplitude of the pinning potential V_0 and misfit parameter δ_{m}. (a) (1×1) C phase; (b) $c(2 \times 2)$ C phase; (c) (2×1) C phase; (d) hexagonal (full) I phase and (e) I phase with domain walls near the $c(2 \times 2)$ C phase.

phase, where they form a superstructure with periodicity twice that of the pinning potential along the principal directions and a $c(2\times1)$ phase where the superstructure has lattice periodicity twice the pinning potential along one of the directions. In addition, there are incommensurate phases, where $\psi(\vec{x})$ forms a hexagonal periodic structures incommensurate with the pinning potential as in Fig. 4.10(d) or a structure of domain walls separating commensurate regions as in Fig. 4.10(e).

The results of extensive numerical calculations using the dynamical equation (4.14) are summarized in the phase diagram in Fig. 4.11 for $-0.5 \leq \delta_{\rm m} \leq -0.225$ and in Fig. 4.12 for $-0.2 \leq \delta_{\rm m} \leq 0.4$. The transitions between the different phases were determined from the change in the structure factor. Qualitatively the phase diagrams calculated at constant average density in Sec. 4.1 and the one calculated at constant chemical potential μ are similar in the range of mismatches $-0.2 \leq \delta_{\rm m} \leq 0.4$, though the absolute values of pinning amplitudes are different. For the range of mismatches $-0.5 \leq \delta_{\rm m} \leq -0.225$ the commensurate phase $(2\sqrt{2}\times\sqrt{2})$ was not found for the unconserved case. This is because the range of stability of the c(2×1) and $(2\sqrt{2}\times\sqrt{2})$ phases depends on the average density, $\bar{\psi}$.

4.2.3 Finite-temperature phase diagram

We studied the influence of thermal fluctuations and lattice mismatch near the simplest commensurate structures, the (1×1) and $c(2\times2)$ commensurate phases, using the MC method described in Sec. 4.2.1. The phase diagrams were obtained by monitoring the behavior of the structure factor and specific heat as a function of temperature and lattice misfit. First, the structure factor $S(\vec{k})$ was calculated from the positions $\vec{R}_j$ of the local peaks in the field $\psi(x,y)$ as

$$S(\vec{k}) = \langle \sum_{j,j'=1}^{N_P} \frac{1}{N_P} e^{-i\vec{k}\cdot(\vec{R}_j-\vec{R}_{j'})} \rangle, \tag{4.15}$$

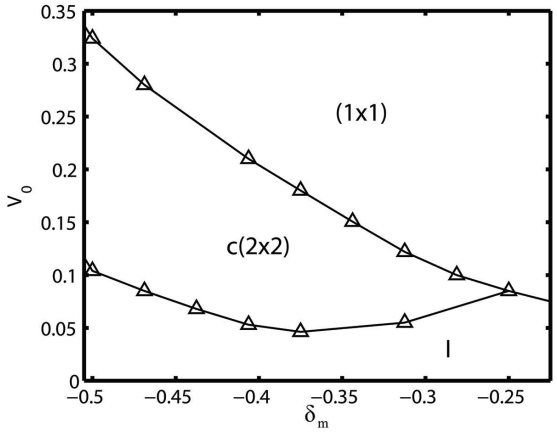

Figure 4.11: Ground state phase diagram in terms of the pinning strength V_0 and the lattice mismatch $\delta_{\rm m}$ for $-0.5 \leq \delta_{\rm m} \leq -0.225$

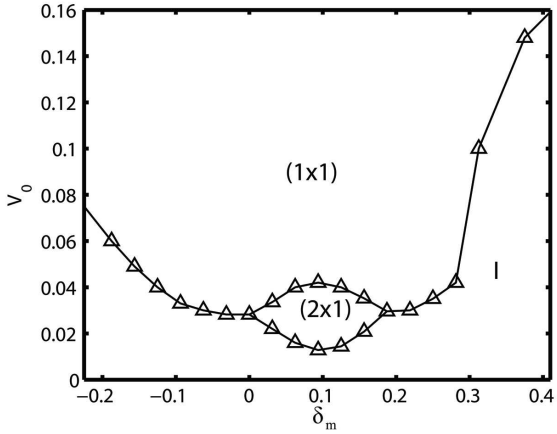

Figure 4.12: Ground state phase diagram in terms of the pinning strength V_0 and mismatch $\delta_{\rm m}$ for $-0.2 \leq \delta_{\rm m} \leq 0.4$.

where N_p is the number of peaks. To locate the peak positions $\vec{R}_j$ for each configuration of $\psi(x,y)$ we implemented a computer algorithm [32] to find the local maxima in $\psi(x,y)$ based on a particle location algorithm used in digital image processing [15]. Alternatively, a structure factor can also be defined directly from the field $\psi(x,y)$ as

$$S_\psi(\vec{k}) = \frac{1}{L^2}\langle|\psi(\vec{k})|^2\rangle, \tag{4.16}$$

where $\psi(\vec{k})$ is the Fourier transform of $\psi(\vec{x})$. While the two expressions give similar results the former expression is better for characterizing a structural phase transition as it includes only the ordering of the lattice and does not simultaneously include fluctuations in the amplitude of ψ as the latter expression does. The results described here were obtained using the definition in Eq. (4.15). Second, the specific heat c was calculated directly from the average energy as $c = (1/L^2)(d\langle H\rangle/dT)$ and from the fluctuation relation

$$c = \frac{1}{L^2T^2}(\langle H^2\rangle - \langle H\rangle^2). \tag{4.17}$$

We checked that these two different ways of calculating c gave the same results, which indicates that the system is properly equilibrated at a given temperature.

Figs. 4.13(a) and 4.13(b) show the behavior of the scaled structure-factor peak $S(k_m)/N_p$ and specific heat c as a function of temperature for the (1×1) and $c(2\times2)$ commensurate phases. Here k_m is the magnitude of the wave-vector corresponding to the local maximum in $S(\vec{k})$. For the (1×1) phase, $S(k_m)/N_p$ in Fig. 4.13(a) decreases and broadens with temperature but does not disappear at the highest temperature where a liquid-like phase is expected. Also, there is no peak in the corresponding specific heat in Fig. 4.13(b). This indicates that the (1×1) phase does not melt into a liquid-like phase via a phase transition, instead there is a smooth crossover from a low temperature highly ordered phase to a high temperature phase where the pinning potential still induces some order in the peak pattern of $\psi(\vec{x})$. This behavior is expected on theoretical grounds [2, 19] since in this case the pinning potential has the same symmetry as the commensurate phase and acts as a constant external field on the displacement order parameter. On the other hand, for the $c(2\times2)$ commensurate phase, $S(k_m)/N_p$ in Fig. 4.13(a) drops sharply near the

temperature where there is a peak in the corresponding specific heat in Fig. 4.13(b) and this behavior is associated with the melting of the ordered structure into a liquid-like phase.

The phase diagrams obtained near the (1×1) and $c(2 \times 2)$ commensurate phases as a function of misfit, strength of pinning potential and temperature are shown in Figs. 4.14 and 4.15, respectively. In addition to the melting transitions, there are also commensurate-incommensurate transitions from the $c(2\times2)$ to I phases and from $c(2\times2)$ to (1×1) phases which are identified by the change in the peak patterns in the structure factor. A striking feature of the phase diagram is its topology, which is strongly dependent on the type of C phase. This agrees qualitatively with theoretical predictions from simplified models [2, 19]. However, the present calculations were not sufficiently accurate to determine the joining of the transition lines near the incommensurate phases in Figs. 4.15(a) and (b). Hence, we were unable to investigate the theoretical predictions [19, 50] for the existence of an intermediate liquid phase between the I and C phases at finite temperature near the $c(2 \times 2)$ commensurate phase.

In addition to the topology of the phase diagram, the nature of the phase transitions between the different phases is of particular interest. We investigated in detail the critical behavior for the simplest case, corresponding to the melting transition of the $c(2 \times 2)$ commensurate phase as a function of the temperature. From symmetry considerations and Landau free-energy expansions [51], one expects that the critical behavior should be in the Ising universality class. To verify if the phase field crystal model provides a correct description of this behavior, we performed a finite-size scaling analysis of the melting of the $c(2 \times 2)$ phase as a function of temperature, for a fixed value of misfit $\delta_{\rm m} = -0.5$. Calculations were performed for increasing system sizes for the specific heat, structure factor and a suitable dimensionless Binder ratio [7]. We define the Binder ratio $U_L(T)$ as

$$U_L = 2 - \frac{\langle|\rho(k_m)|^4\rangle}{\langle|\rho(k_m)|^2\rangle^2}, \tag{4.18}$$

where the order parameter $\rho(k_m)$ is the Fourier transform of the of density of local peaks

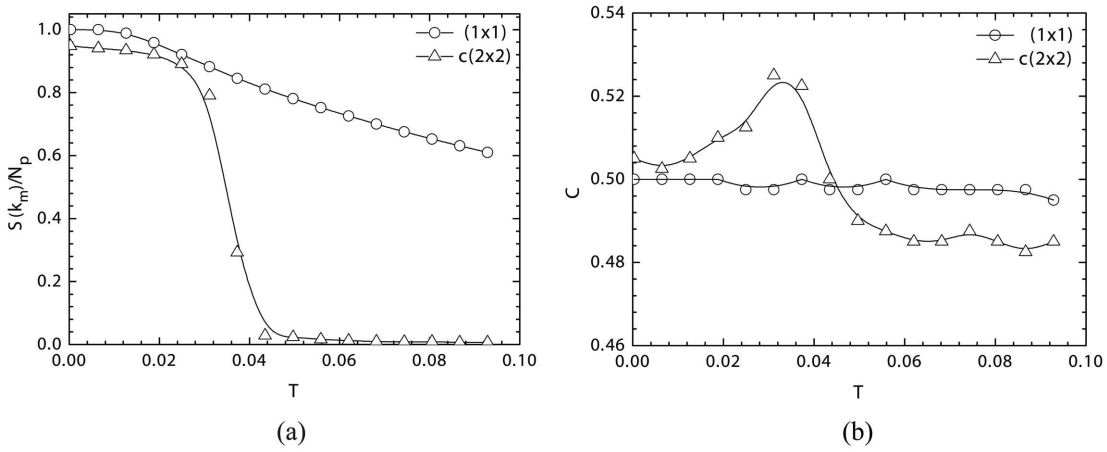

Figure 4.13: Temperature dependence of the scaled structure-factor peak $S(k_m)/N_p$ (a) and specific heat c (b) for the (1×1) commensurate phase ($\delta_{\rm m} = 0$, $V_0 = 0.10$) $c(2 \times 2)$ commensurate phase ($\delta_{\rm m} = -0.5$, $V_0 = 0.275$). Here k_m is the wave vector of the corresponding ordered structure.

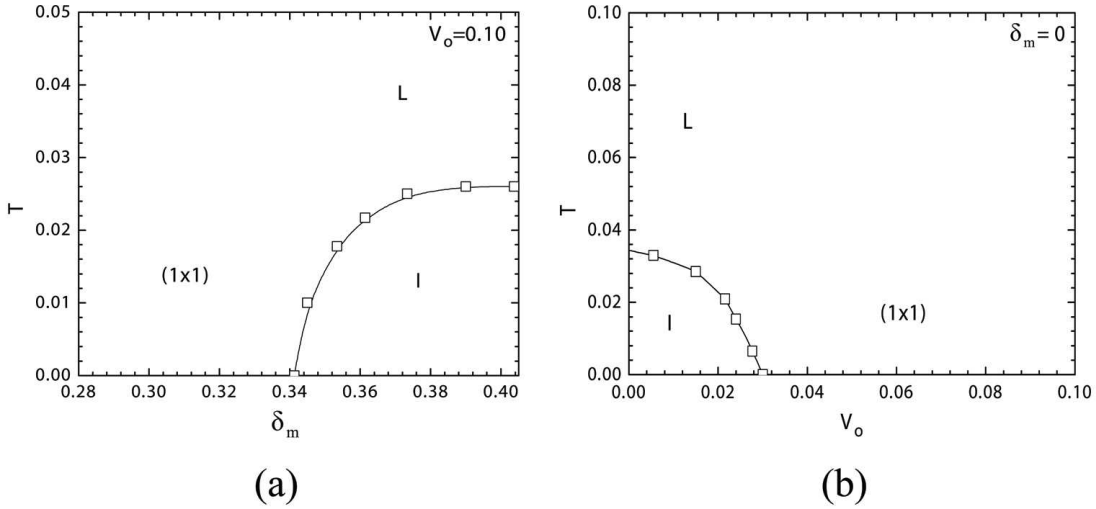

Figure 4.14: Phase diagrams near the (1×1) commensurate phase. (a) at fixed pinning strength V_0 and (b) at fixed misfit $\delta_{\rm m}$.

in the field $\psi(x, y)$ at $\vec{R}_j$

$$\rho(k_m) = \frac{1}{N_P} \sum_{j=1}^{N_P} e^{-i\vec{k}_m \cdot \vec{R}_j}, \tag{4.19}$$

evaluated at the wave vector k_m corresponding to the local maximum of the structure factor $S(k)$. The finite-size behavior of U_L provides an accurate determination of the critical temperature T_c and an estimate of the thermal critical exponent ν which characterizes the divergent correlation length, $\xi \propto |T - T_c|^{-\nu}$, near the transition [7, 8]. In the high temperature disordered phase, the real and imaginary parts of $\rho(k_m)$ fluctuate with a Gaussian distribution leading to $U_L \to 0$ while at low temperature there is long-range order with $\langle \rho(k_m) \rangle \neq 0$ and therefore $U_L \to 1$ for $L \to \infty$. At the critical temperature T_c, the ratio U_L becomes independent of the system size L and therefore plots of $U_L(T)$ as a function of temperature for different systems sizes should cross at the same point, corresponding to the critical temperature T_c of the system in the thermodynamic limit. In the scaling regime sufficiently close to T_c, the dimensionless $U_L(T)$ should satisfy the scaling form

$$U_L(T) = \bar{U}((T - T_c)L^{1/\nu}), \tag{4.20}$$

where $\bar{U}(x)$ is a scaling function. Since the slope $(\partial U_L(T)/\partial T)$ evaluated at T_c is proportional to $L^{1/\nu}$, an estimate of ν can be obtained [8] from a log-log plot of this quantity against L.

Fig. 4.16(a) shows the temperature behavior of U_L for different system sizes. Although the curves do not cross precisely at the same point, for the three largest system sizes the curves intersect approximately at $T_c \approx 0.03599(20)$. The lack of intersection at a common point should be due to statistical errors and corrections to scaling. Fig. 4.16(b)0 shows a log-log of $\delta U_L(T)/\delta T$ evaluated at the estimated T_c against L from where we obtain $1/\nu = 1.1(1)$. This estimate of ν is in agreement with the exact value for the thermal exponent of the two-dimensional Ising model, $\nu = 1$.

The finite-size behavior of the specific heat c is also consistent with the Ising universality class, where the specific heat exponent is $\alpha = 0$. Fig. 4.17(a) shows the temperature behavior of the specific heat for the different systems sizes. From finite-size scaling,

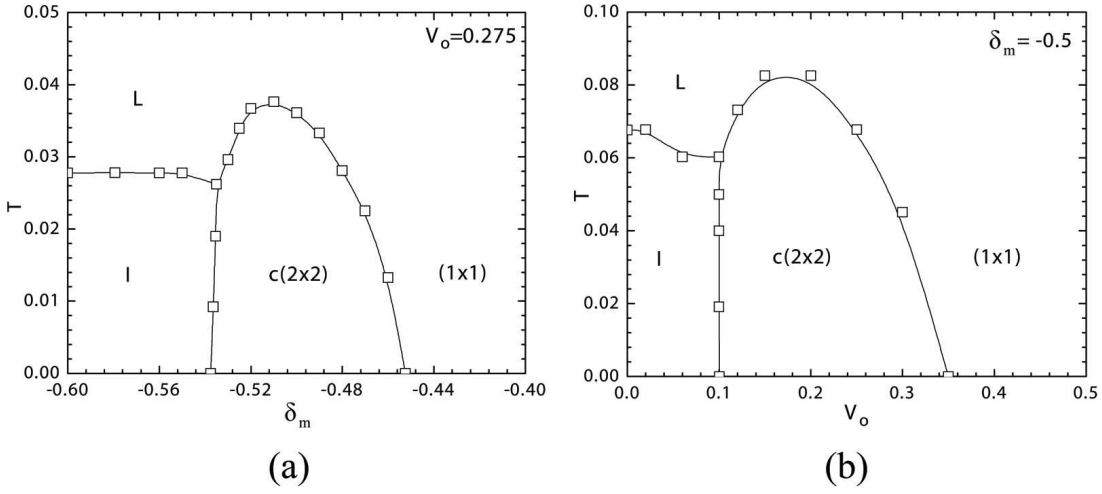

Figure 4.15: Phase diagrams near the $c(2 \times 2)$ commensurate phase. (a) at fixed pinning strength V_0 and (b) at fixed misfit $\delta_{\rm m}$.

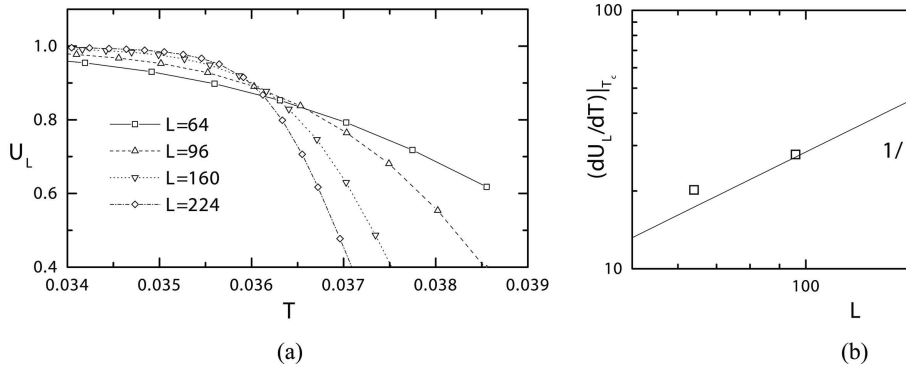

Figure 4.16: (a) Temperature dependence of the Binder ratio $U_L(T)$ for different system sizes L, near the melting transition of the $c(2 \times 2)$ commensurate phase at $\delta_{\rm m} = -0.5$ and $V_0 = 0.275$; (b) Estimate of the thermal critical exponent ν from the log-log plot of $\frac{\partial}{\partial T} U_L(T)$ at T_c against L for the three largest system sizes.

the maximum of c should scale as $L^{\alpha/\nu}$, which corresponds to a logarithmic behavior $C_{max} \propto \log L$, if $\alpha = 0$. Fig. 4.17(b) shows that the linear-log plot of the specific heat maximum c_{max} against L seems to be consistent with a logarithmic behavior for the three largest system sizes.

The correlation function exponent η can also be estimated from the expected finite-size behavior of the structure factor, which should scale as $S(k_m) \propto L^{2-\eta}$ at T_c. Fig. 4.18 shows a log-log plot of $S(k_m)/L^2$ evaluated at the above estimated T_c against L from where we find $\eta = 0.15$. Unlike the above estimates of ν and α, this estimate of η is much smaller than the known exact value for the Ising model, $\eta = 0.25$. This large discrepancy could be due to corrections to scaling. However, to take such corrections into account would require more accurate data and larger system sizes, which is beyond the scope of the present work.

4.3 Random pinning potential in 2D

In the last part of this chapter we present preliminary results regarding the effect of a random pinning potential. In this case the effective potential can be written as a sum of randomly distributed attractive centers:

$$V(\vec{x}) = V_0 \sum_{j=1}^{N_c} v(|\vec{x} - \vec{x}_l|), \tag{4.21}$$

where V_0 represents the coupling amplitude, N_c is number of pinning centers and $\vec{x}_l$ is the position of the l center chosen from a set of uniform distributed numbers. The strength of the interaction is determined by V_0, the density of pinning centers $\rho_c = N_c/S$ and the width of the $v(|\Delta\vec{x}|)$, σ_v. The function $v(|\Delta\vec{x}|)$ decreases very fast to zero for $|\Delta\vec{x}| > \sigma_v$. For all calculations presented in here, we set $\sigma_v \simeq a_t/7$. In order to make sure that there is only one pinning center per pinned maxima the distance between pinning centers was not allowed to be less than the lattice constant, a_t, of the triangular phase.

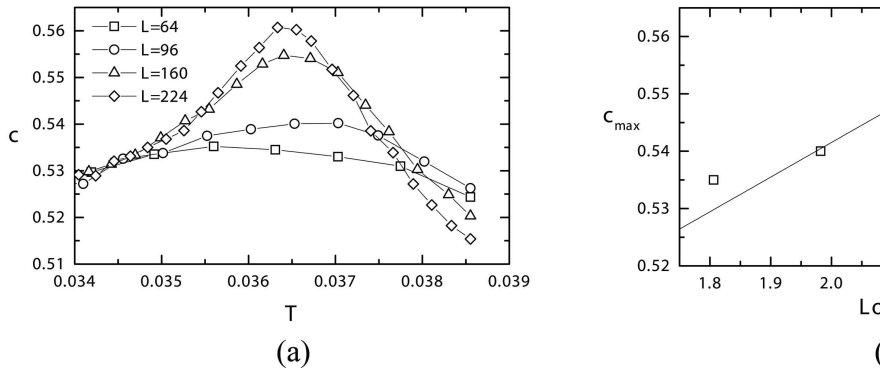

Figure 4.17: (a) Temperature dependence of the specific heat c for different system sizes L, near the melting transition of the $c(2 \times 2)$ commensurate phase at $\delta_{\rm m} = -0.5$ and $V_0 = 0.275$; (b) Specific heat maxima c_{max} in a linear-log plot indicating a logarithmic behavior as a function of L for the three largest systems sizes.

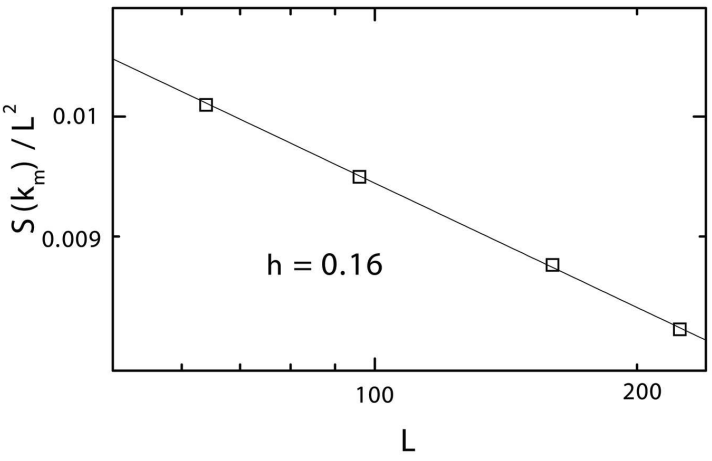

Figure 4.18: Estimate of the correlation function exponent η from the log-log plot of $S(k_m)/L^2$ at T_c against L for the three largest systems sizes.

The free energy of the system is given by Eq. (4.1), while the dynamics are conserved and follow the Eq. (4.3). The numerical calculations were done using the same method that was used to study the effect of a periodic pinning potential. This model offers a good description of vortex lattice in type II superconductors and can be connected to real materials by fitting the elastic constants.

The positional ordering of the system can be characterized by an order parameter defined as

$$\zeta^{\psi}_{pos} = \frac{1}{\sqrt{S}}\langle| \int d\vec{x} \exp{(i\vec{G}_t \cdot \vec{x})}\psi(\vec{x})|\rangle, \tag{4.22}$$

where S is the area of the system, G_t is a inverse reciprocal lattice vector of the triangular phase and the average is done over different realizations of the pinning potential. Information about the structure of the system can be obtained from the structure factor

$$S_{\psi}(\vec{k}) \;\; = \;\; \frac{1}{S}\langle| \int d\vec{x} \exp{(i\vec{k} \cdot \vec{x})}\psi(\vec{x})|^2\rangle. \tag{4.23}$$

The point of transition can be found by investigating the behavior of the positional susceptibility χ^{ψ}, as a function of the pinning strength when the density of pinning centers ρ_c is kept fixed

$$\chi^{\psi}_{pos} \;\; = \;\; S_{\psi}(\vec{G}_t) - \frac{1}{S}\left(\langle| \int d\vec{x} \exp{(i\vec{G}_t \cdot \vec{x})}\psi(\vec{x})|\rangle\right)^2. \tag{4.24}$$

A discontinuity or a divergence of this function indicates a phase transition at $V_0 = V_c$. We expect a strong dependence of V_c of the system size $S = l_x dx \times l_x dx$,

$$|V_c(l_x) - V_c(\infty)| \propto l_x^{\xi}. \tag{4.25}$$

In addition to the positional order parameters ζ^{ψ}_{pos}, an order parameter for orientational symmetry also has to be defined. There exist phases in which there is orientational symmetry but no positional symmetry, for instance, the hexatic phase [13]. The hexatic phase has a sixfold orientational symmetry, but no positional symmetry. The hexatic phase would be characterized by the vanishing of the positional symmetry before the orientational. In the hexatic phase, orientational order decays algebraically while the positional order decays exponentially.

The maxima of the field ψ are lattice sites where the real particle spend most of the time; a lattice site was present at position (i, i') if $\psi(i, i')$ was greater than or equal to its nearest neighbors and $\psi(i, i')$ was greater than $\bar{\psi}$. The nearest neighbors of particle j were found by drawing a circle through particles j, j' and j''. If no other particles were inside the circle, then j' and j'' are nearest neighbors of particle j. The bond-orientational order parameter for the position of the maxima is defined [33] as

$$\zeta_{ori} = \langle \left| \frac{1}{N_p} \sum_{j=1}^{N} \frac{1}{NN_j} \sum_{j'=1}^{NN_j} e^{6i\theta_{jj'}} \right| \rangle, \tag{4.26}$$

where the sum on j is over all the particles and the sum on j' is over the NN_j nearest neighbors of the particle j. $\theta_{jj'}$ is the angle between the line connecting particles j and j' and an arbitrary but fixed reference axis. For the hexagonal phase, ζ_{ori} is equal to unity. The orientational susceptibility, χ^{ψ}, is defined as

$$\chi^{\psi}_{pos} = \langle \left| \frac{1}{N_p} \sum_{j=1}^{N} \frac{1}{NN_j} \sum_{j'=1}^{NN_j} e^{6i\theta_{jj'}} \right|^2 > - < \left| \frac{1}{N_p} \sum_{j=1}^{N} \frac{1}{NN_j} \sum_{j'=1}^{NN_j} e^{6i\theta_{jj'}} \right| \rangle^2. \tag{4.27}$$

4.3.1 Order-disorder transition

In the absence of the pinning potential the system will be in a hexagonal phase as described in Sec. 2.2. For a fixed ρ_c and large enough pinning coupling amplitude V_0 the system will lose the ordering and will be in a disorder state. Two different regimes were investigated, low density of pinning centers, $\rho_c = 0.0032$, and high density of pinning centers, $\rho_c = 0.0095$. In comparison the density of maxima in the unperturbed hexagonal phase is $N_p/S = 0.0222$.

First we present results for low density of pinning centers, $\rho_c = 0.0032$. From Fig. 4.3.1 it can be seen that the positional order is lost before the orientational order. This indicates that the system undergoes a phase transition to an intermediate phase, which has orientational order but no positional order.

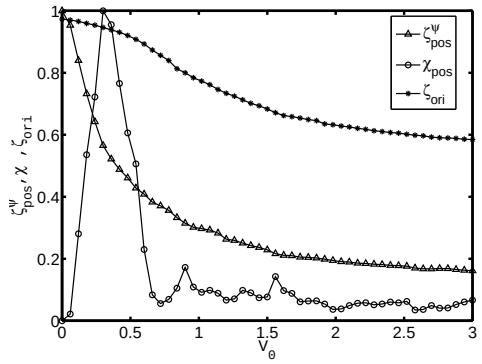

Figure 4.19: The positional order parameter, ζ^{ψ}_{pos}, the positional susceptibility, χ_{pos}, and the orientational order parameter ζ_{ori} as a function of pinning strength V_0 for low density of pinning centers, $\rho_c = 0.0032$. The size of the system was $512 \times 512 dx^2$.

The positional susceptibility has a maximum at the transition point. No other transition was found in the case of low density of pinning centers for the parameters that were investigated. For large pinning strengths the system remains in a hexatic phases.

Similar behavior was found for the case of high density pinning centers. When the pinning strength is increased the positional order parameter decreases to zero, while the orientational order parameter remains finite.

At the point of transition the positional susceptibility has a maximum (Fig. 4.3.1). If the pinning strength is further increased, the local ordering is lost and a phase transition to a fully liquid-like phase occurs. At the point of transition the oriental susceptibility has a maximum (Fig. 4.3.1).

The points of transitions have a strong dependence on the system size, but the data were not accurate enough to perform a finite size scaling. The initial results suggest continuous phase transition, but more calculations (larger systems and more averages) are needed in order to find the exact nature of the phases and the universality class to which they belong.

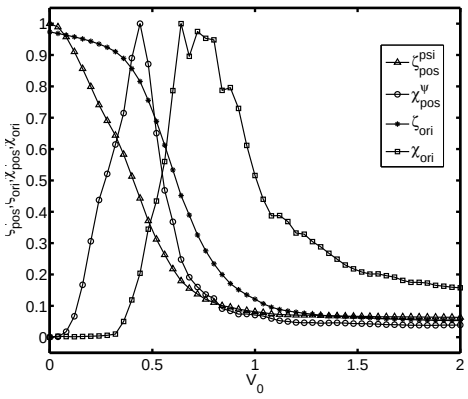

Figure 4.20: The positional order parameter, ζ_{pos}^{ψ}, the positional susceptibility, χ_{pos}, and the orientational order parameter ζ_{ori} as a function of pinning strength V_0 for low density of pinning centers, $\rho_c = 0.0095$. The size of the system was $256 \times 256 dx^2$.

In the next section we present the effect of a driving force on a pinned phase.

5 Driven PFC in external potential

In the present section we focus on the case where the PFC under an external periodic potential without disorder introduced in Sec 4.1 is driven by an external force in the absence of thermal fluctuations [12]. The phase diagram of the PFC model with external periodic pinning potential was mapped in Sec. 4.1. The main focus of the present chapter is on the influence of an external driving force on the pinned C phase, which we study for different values of mismatch and pinning strengths for 1D and 2D systems. As expected, due to the competition between the pinning potential and the driving force there is a depinning transition at f_c for a finite driving force f. We demonstrate that within a certain range of parameters the depinning transitions are continuous, and find that both in 1D and 2D the corresponding power-law exponent is $\zeta = 0.5$ in agreement with the expected value [20, 21, 23, 42]. We also characterize structural changes of the system close to the depinning transition. For large pinning strength transverse depinning transitions in the moving state are also found. Surprisingly, for sufficiently weak pinning potential we find a discontinuous depinning transition with hysteresis even in one dimension although overdamped dynamical equations are used.

5.1 The Phase Field Crystal under a periodic potential and a Driving Force

The response of the system to a driving force can be obtained by including a convective derivative, $\vec{f} \cdot \vec{\nabla}\psi$, to the of the equation of motion (4.3). Thus, the dynamical equation of motion for the phase field is given by

$$\frac{\partial \psi}{\partial \tau} = \nabla^2 \left(\left(r + \left(1 + \nabla^2\right)^2 \right) \psi + \psi^3 + V \right) + \vec{f} \cdot \vec{\nabla}\psi. \tag{5.1}$$

The equation of motion is integrated numerically using the same procedure presented in Chapter 4, with mentioning that for $t \to \infty$ we have $(\partial\psi/\partial t) = constant$. The results

do not change qualitatively when the system size is varied, but the value of the critical force will depend on the size the grid. For the forces considered in this work (typically $\vec{f} = f\hat{x}$), convective term does not change the average value of the density field.

In contrast to the usual classical microscopic characterization of particle positions and velocities, the measurement of an average drift velocity in response to an external driving force $\vec{f}$ requires some discussion. In the PFC model the maxima of the density field that defines the lattice structure cannot always be interpreted as individual particles, since vacancies may be present in the system. The conservation law in the model concerns the local density field, not the number of maxima in the field. This becomes evident in the driven PFC model, where the motion of the density field close to depinning may be more akin to flow in a continuous medium than the motion of discrete particle-like objects. Thus, defining the drift velocity in terms of the density field maxima is computationally more demanding to implement. We have found that measuring the drift velocity v_d from the rate of change of the gradient of the density field gives consistent results, in absence of thermal fluctuations. We have used the following definition

$$v_d \equiv \left\langle \langle |\partial\psi/\partial t| \rangle_{\vec{x}} \,/\, \langle |\partial\psi/\partial x| \rangle_{\vec{x}} \right\rangle_t , \tag{5.2}$$

where the subscripts $\vec{x}$ and t in the brackets denote averaging over space and time, respectively. Alternative definitions were also considered, $\langle \langle |\partial\psi/\partial t| \rangle_{\vec{x}} \rangle_t$, $\left\langle \sqrt{\left\langle (\partial\psi/\partial t)^2 \right\rangle_{\vec{x}}} \right\rangle_t$, and $\left\langle \sqrt{\left\langle (\partial\psi/\partial t)^2 \right\rangle_{\vec{x}}} \Big/ \sqrt{\left\langle (\partial\psi/\partial x)^2 \right\rangle_{\vec{x}}} \right\rangle_t$, but the results were qualitatively identical.

Although the definition of the drift velocity v_d according to Eq. (5.2) can be used to determine the velocity response along the direction of the driving force, it is not particularly useful in the study of the response in the transverse direction since it is not a vector quantity. In order to study the transverse response it is more convenient to determine the average velocity directly from the positions of the local peaks in $\psi(\vec{x})$. We used the same method to locate the peaks as in Sec. 4.2. The drift velocity for the lattice of density peaks is obtained from the peak velocities $\vec{v}_i$ as

$$\vec{v}_P = \left\langle \frac{1}{N_P} \sum_{i=1}^{N_P} \vec{v}_i(t) \right\rangle_t , \tag{5.3}$$

where N_P is the number of peaks. We find that the definitions of the velocity from Eqs. (5.2) and (5.3) give consistent results for the longitudinal depinning in the absence of thermal fluctuations. However, in the presence of thermal fluctuations only the definition from the peak velocities (5.3) is able to separate the contribution to the drift velocity due to the driving force from thermal noise.

5.2 Driving in one dimensional systems

Next we investigate the influence of an external force on the 1D commensurate phase. For this purpose, the parameters are chosen such that $r = -1/4$, and $\bar{\psi} = 0$. Depending on the values of the mismatch and pinning strength different behavior is found when the driving force is added. Several values of mismatch between 0.3125 and -0.50 were investigated. For $\delta_{\rm m} \gtrsim -0.3$ two types of depinning are present, discontinuous and continuous. For values of the pinning strength close to the I-C phase transition, the depinning transition is discontinuous. The dependence of the drift velocity as a function of the driving force exhibits a hysteresis (see Fig. 5.1(a)). The gap $\Delta f_c = f_c^{in} - f_c^{de}$ decreases when the pinning strength increases (Fig. 5.1(b)), which indicates that the transition becomes continuous for large enough V_0.

Note that for $\delta_{\rm m} \lesssim -0.3$ the depinning transition of a C pinned phase is continuous for all values of the pinning strength, while for $\delta_{\rm m} \gtrsim -0.3$ only for values of pinning strength above a certain threshold. In Fig. 5.2, we show the behavior of a continuous depinning transition for $\delta_{\rm m} = 0.3125$, $V_0 = 0.11$. The dependence of the drift velocity on the force follows a power law $v_d \propto (f - f_c)^{\zeta}$, as can be seen in Fig. 5.2. The exponent ζ does not depend of the pinning strength and it is equal to 0.50 ± 0.03 in all cases studied here. This result can be understood as follows. When the pinning potential is periodic and large in magnitude the neighboring phases are weakly coupled and the system should behave as a single particle in a periodic potential [20, 21, 23, 42]. This effective single particle behavior, which is expected to describe the threshold behavior for a commensurate phase

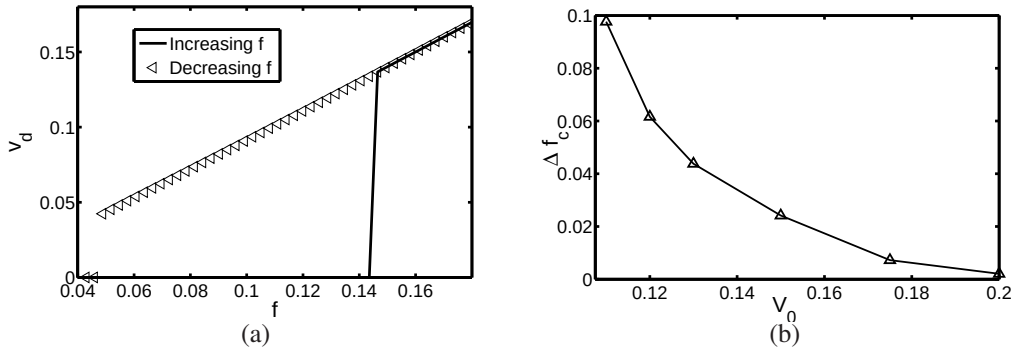

Figure 5.1: (a) Discontinuous depinning of the commensurate phase for a relatively low pinning strength ($\delta_{\rm m} = 0.3125$, $V_0 = 0.11$). (b) Dependence of Δf_c on V_0 for $\delta_{\rm m} = 0.3125$.

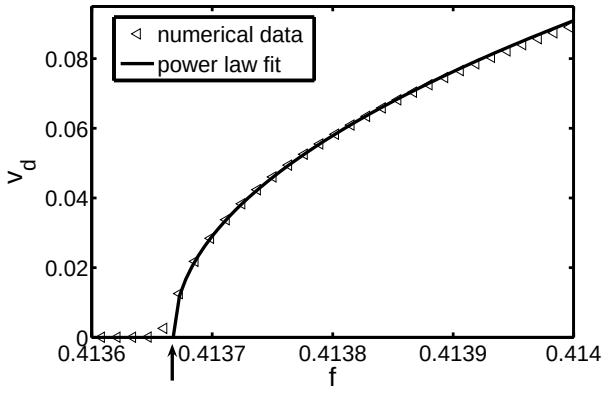

Figure 5.2: Continuous depinning transition for relatively high pinning strength ($\delta_{\rm m} = 0.3125$ and $V_0 = 0.250$). The arrow marks the value of the critical depinning force. The triangles represent the numerical data while the continuous line is a fit to $(f - f_c)^{\zeta}$. The best fit is obtained for the exponent $\zeta = 0.50 \pm 0.03$.

in absence of defects, is independent of the dimension, leading to a depinning exponent $\zeta = 1/2$ [20, 21, 23, 42]. We also find that the critical force increases with the pinning strength and for $\delta_{\rm m} \gtrsim -0.3$ has linear dependence on the pinning strength, while for $\delta_{\rm m} \lesssim -0.3$ its dependence on pinning becomes sub-linear. Finally, we also note that for large driving forces $f \gg f_c$ the system is totally depinned and the dependence of the drift velocity on the force follows Eq. (1.2) with a linear dependence.

5.3 Driving in two dimensional systems

5.3.1 Nonlinear Response of the (1×1) phase

We now turn to the influence of an external driving force for the pinned, commensurate (1×1) and $c(2 \times 2)$ phases. Depending on the values of $\delta_{\rm m}$ and V_0, for both phases we find both discontinuous and continuous depinning transitions. For $\delta_{\rm m} \geq -0.2$ and $V_0 \geq 0.09$ both continuous and discontinuous depinning mechanisms were found for the commensurate (1×1) phase. For smaller values of the pinning strength close to the IC transition, only discontinuous depinning transitions were found. Similar to the 1D case, we identify two values of the critical forces for a discontinuous depinning, namely f_c^{in} for when the force is increased and f_c^{de} when the force is decreased back to zero. Figure 5.3(a) shows the velocity dependence with respect to the applied force for a discontinuous transition. We have also tested the effect of thermal fluctuations here and find that for low temperatures the hysteresis remains unchanged up to some value which depends on the mismatch and pinning strength. The gap $\Delta f_c = f_c^{in} - f_c^{de}$ for a given $\delta_{\rm m}$ decreases as the pinning strength is increased (Fig. 5.3(b)). Finally, when the gap Δf_c vanishes the depinning transition becomes continuous. In this regime we find that the sliding velocity follows a power low $v_d \propto (f - f_c)^{\zeta}$ (Fig. 5.4), consistent with $\zeta = 0.5$ in all cases studied here as in the 1D case. We note that for $\delta_{\rm m} \leq -0.2$ only continuous depinning transitions were found for all values of the pinning strength.

The depinning transitions are accompanied by structural changes. In the case of discontinuous depinning the system will be in commensurate (1×1) phase, below the critical threshold, and in a distorted hexagonal just above the critical threshold. (Figs. 5.5). In the case of continuous depinnig the system will remain in a square phase (Fig. 5.6). In both cases, for very large forces the system will be totally depinning along driving force and the velocity is direct proportional to the applied force.

5.3.2 Nonlinear Response of the $c(2 \times 2)$ phase

Similar to the (1×1) phase, the commensurate $c(2 \times 2)$ phase also exhibits both discontinuous and continuous depinning. For low value of pinning strength discontinuous depinning transition was found (Fig. 5.7), while for large values of the pinning strength the depinning becomes continuous (Fig. 5.8) with the exponent $\zeta = 0.5$. In the case of discontinuous depinning the system will be in commensurate $c(2 \times 2)$ phase, below the critical threshold, and in a distorted hexagonal just above the critical threshold (Figs.5.9). In the case of continuous depinning the system will remain in a square phase just above the critical threshold (Fig. 5.10). In both cases, for very large forces the system will be totally depinned along driving force and the velocity is direct proportional to the applied force.

While for the cases presented here the structural changes occur when the system starts to depin, it is also possible for changes to occur for forces below the critical threshold. For some values of the mismatch and pinning strength, if the force is rotated 45 degrees the $c(2 \times 2)$ phase will change first to a (1×1) phase from which the systems depins continuously as described before. Other force induced transitions between commensurate phases with no sliding are also possible.

The hysteretic behavior of the depinning transition found for sufficiently small pinning strength V_0 and the critical exponent ξ for the continuous transition are confirmed by

calculations of peak velocity v_p from Eq. (5.3). For large V_0 where there is no hysteresis and the behavior v_p show a depinning transition at a critical force f_c. A power-law fit of the velocity near f_c gives an exponent $\zeta = 0.52 \pm 0.03$ which is consistent with the estimate using the velocity definition in Eq. (5.2).

The determination of the velocity response from the peak positions allows us also to study the response to an additional force f_y applied perpendicular to the longitudinal force f_x. For $f_x >> f_c$ the longitudinal velocity v_x is proportional to the force since in the moving state the external pinning potential in the direction of the force appears as a time dependent perturbation in a reference system co-moving with the lattice, with a vanishing time average [16]. However, the pinning potential remains static in the transverse direction [16]. One then expects that for sufficiently larger pinning strength, a transverse depinning transition is possible for increasing force f_y while f_x is kept fixed. Fig. 5.11(a) shows the behavior of the transverse velocity component v_y, when an increasing f_y is applied in the moving state with fixed $f_x > f_c$ in Fig. 5.8(a). The transverse critical force f_{yc} decreases with the longitudinal force f_x and vanishes near the longitudinal depinning transition f_c, as shown in Fig. 5.11(b).

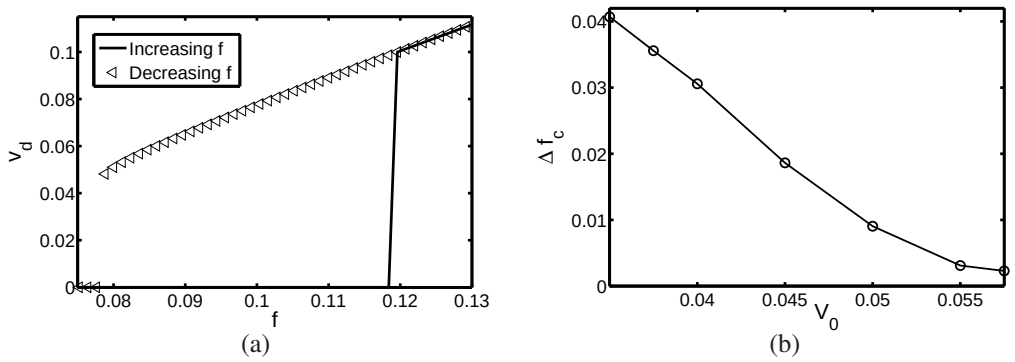

Figure 5.3: (a) The variation of the velocity with respect to the external force for a discontinuous transition for the commensurate (1×1) phase ($\delta_{\rm m} = 0.125, V_0 = 0.0350$) and (b) the variation of the gap Δf_c vs V_0 for the same mismatch $\delta_{\rm m} = 0.125$.

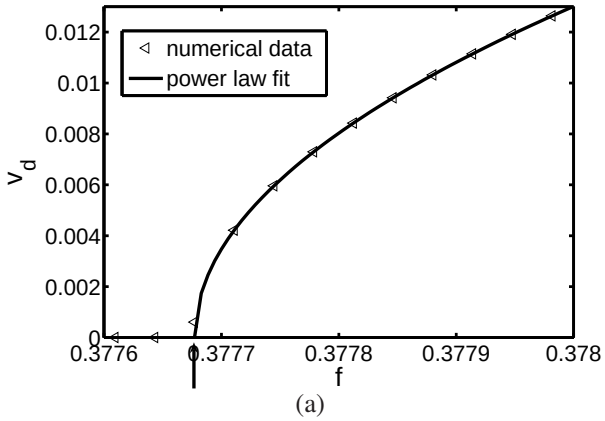

Figure 5.4: Dependence of the velocity on the external force for a continuous transition for the (1×1) phase ($\delta_{\rm m} = 0.125, V_0 = 0.0900$). The vertical arrow marks the critical force f_c. The triangles represent the numerical data, while the continuous line is a power-law fit with $\zeta = 0.50 \pm 0.03$.

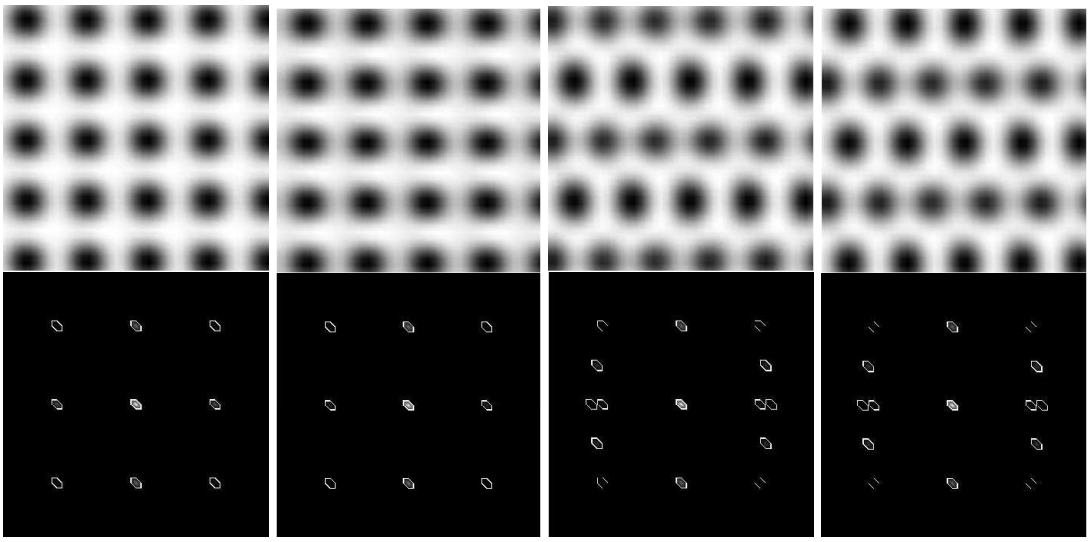

(a) (b) (c) (d)

Figure 5.5: Change of the lattice structure (upper panels) and the corresponding structure factor (lower panels) with the applied force for $\delta_{\rm m} = 0.125, V_0 = 0.0350$, where depinning is discontinuous. Image (b) corresponds to $f = 0.11$ with a non-moving initial configuration, while for (c) the applied force is the same but the initial configuration is a moving one. The case (a) $f = 0.07$, (d) $f = 0.13$ are outside of the hysteresis region and same result is obtained with moving or non-moving initial configuration.

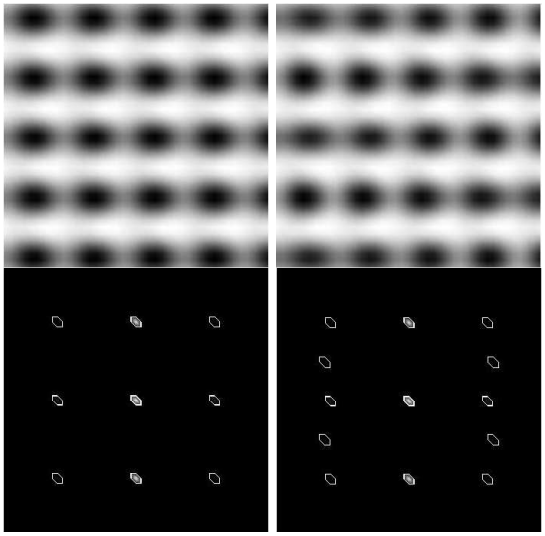

(a) (b)

Figure 5.6: Change of the structure factor with the applied force for $\delta_{\rm m} = 0.125, V_0 = 0.0900$, where depinning is continuous. The images correspond to (a) $f = 0.3776$ (before the depinning transition marked by the vertical arrow in Fig. 5.4(a)), (b) $f = 0.3782$ (after the depinning transition).

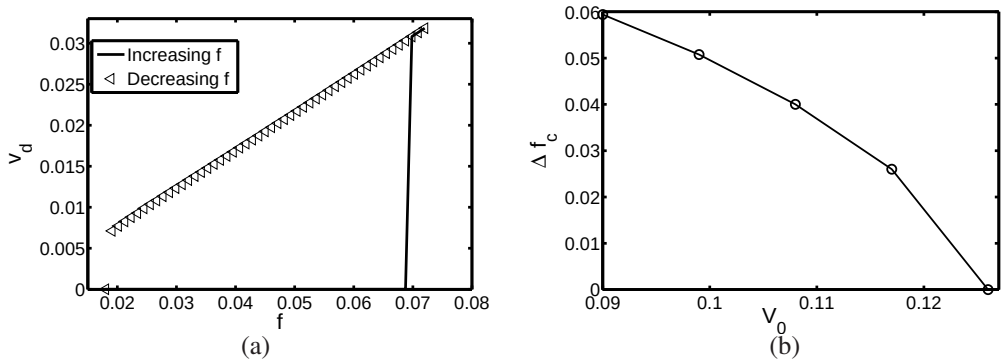

(a) (b)

Figure 5.7: (a) The variation of the velocity with respect to the external force for a discontinuous transition for the c(2×2) ($\delta_{\rm m} = -0.50, V_0 = 0.099$) and (b) Δf_c vs V_0 for $\delta_{\rm m} = -0.50$.

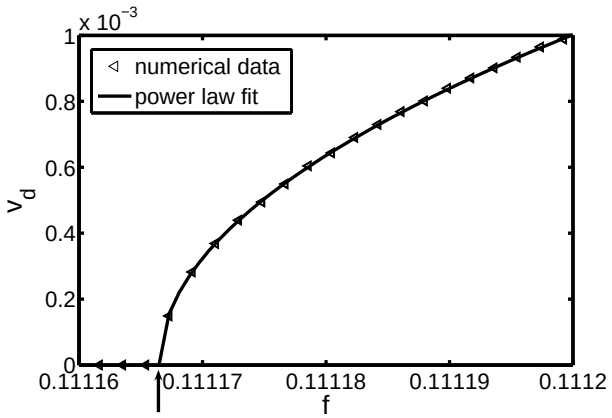

(a)

Figure 5.8: The variation of the velocity with respect to the external force for a continuous transition ($\delta_{\rm m} = -0.50, V_0 = 0.207$) for the c$(2 \times 2)$ and the corresponding power law fit. The vertical arrow marks the value of the critical depinning force.The triangles represent the numerical data, while the continuous line the power law fit with $\zeta = 0.50 \pm 0.03$.

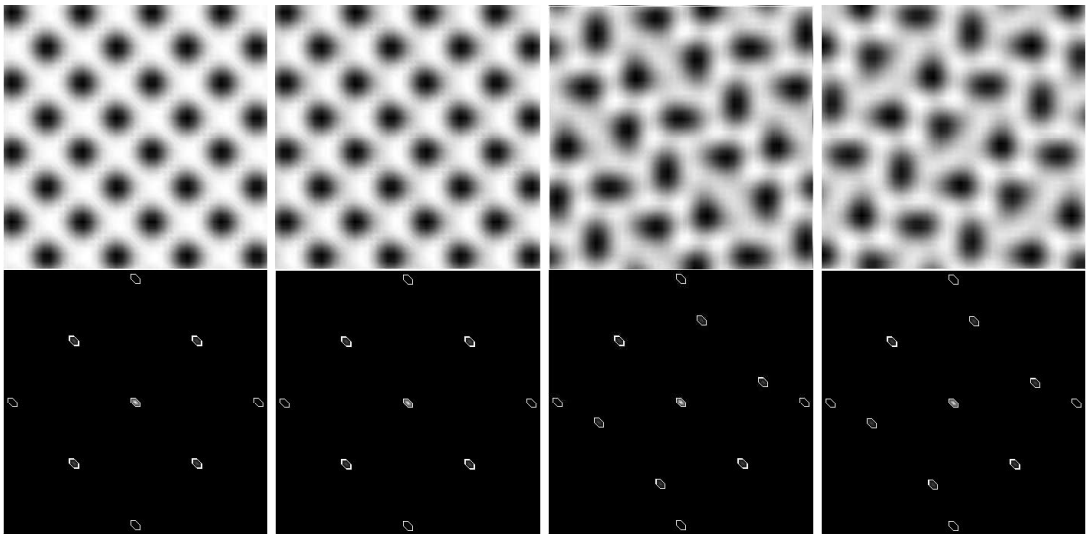

(a) (b) (c) (d)

Figure 5.9: Change of the lattice structure (upper panels) and the corresponding structure factor (lower panels) with the applied force for $\delta_{\rm m} = -0.5, V_0 = 0.099$ for the c(2×2) ,where depinning is discontinuous. Image (b) corresponds to $f = 0.10504$ with a non-moving initial configuration, while for (c) the applied force is the same but the initial configuration is a moving one. The cases (a) $f = 0.018$, (d) $f = 0.13$ are outside of the hysteresis region and same result is obtained with moving or non-moving initial configuration.

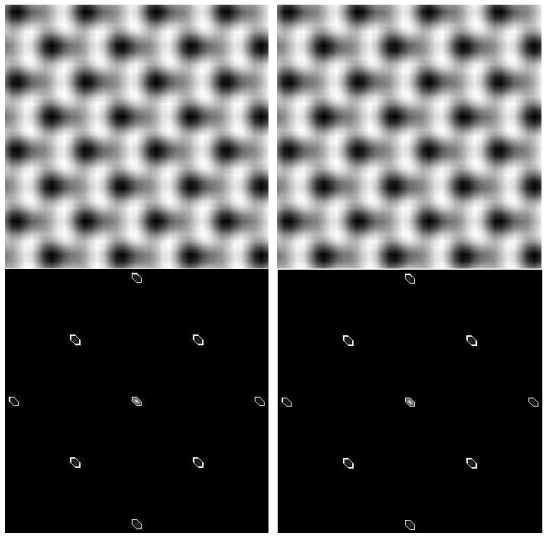

(a) (b)

Figure 5.10: Change of the structure factor with the applied force for $\delta_{\rm m} = -0.50, V_0 = 0.207$ for the c(2×2), where depinning is continuous. The images correspond to (a) $f = 0.1111664528$ (right before the depinning transition indicated by the vertical arrow in Fig. 5.8(a), (b) $f = 0.1111672800$ (right after the depinning transition).

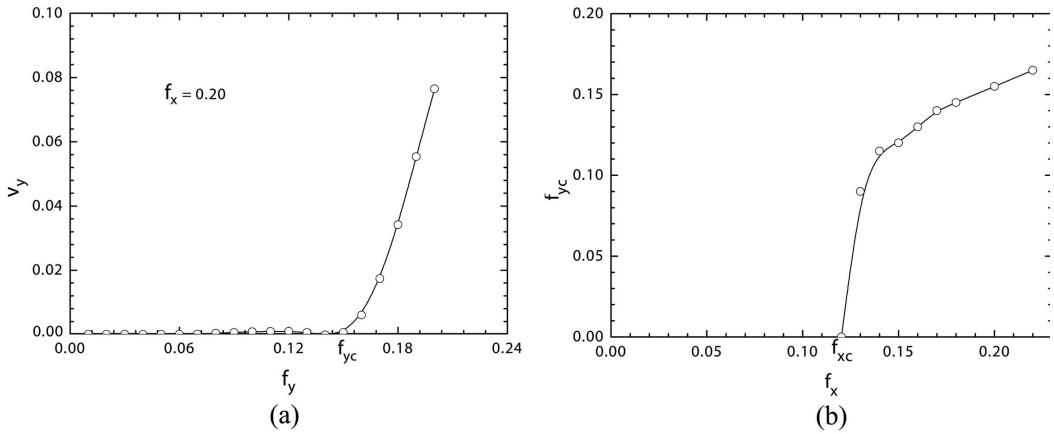

Figure 5.11: (a) v_y as a function of an additional force f_y in the transverse direction, with f_x fixed. (b) Critical transverse force f_{yc} as a function of the longitudinal force f_x. Results for $V_0 = 0.275$, $\delta_m = -0.5$.

6 Conclusions

In this thesis we have presented a comprehensive study of the static and dynamic properties of some lattice systems under the influence an external potential and driving force. These properties were studied using the recently developed Phase Field Crystal model [17] in the presence of an external pinning potential [10, 11] and a driving force in Ref. [12]. As the model naturally incorporates both elastic and plastic deformations, it provides a continuum description of lattice systems such as adsorbed atomic layers or 2D vortex lattices, while still retaining the discrete lattice symmetry of the solid phase. The main advantage of the model as compared to traditional approaches is that despite retaining spatial resolution on an atomic scale its temporal evolution naturally follows diffusive time scales. Thus the numerical simulation studies of the dynamics of the systems can be achieved over realistic time scales many order of magnitudes over the microscopic atomic models. In this work we have exploited this method to determine the phase diagram in one and two dimensions as a function of lattice mismatch and pinning strength. The results were found be consistent with simulations of atomistic models of pinned overlayers on surfaces.

The pinning potential was chosen such that it allows the occurrence of both C and I phases as ground states of different symmetries in the model. The different C phases were presented in detail and the phase diagrams as function of pinning strength and lattice mismatch between the pinning potential and the PFC were mapped out for both 1D and 2D cases analytically and numerically in the absence of thermal fluctuations. Depending on the mismatch, the transition from I phase to C phase was found to both continuous and discontinuous in 1D while for the 2D case was found to be discontinuous for all range of mismatches that were investigated. The transition between different C phases is expected to be continuous due to the fact that they the same symmetry. The influence of the thermal fluctuations was also studied. The results revealed that the model has a rich phase diagram, which includes commensurate, incommensurate, and liquid like phases

with a topology dependent on the type of ordered structure. In particular, a finite-size scaling analysis of the melting transition for the c(2×2) commensurate phase shows that the thermal correlation length exponent ν and specific heat behavior are consistent with the Ising universality class. In the 2D we studied also the effect of randomly and uniformly distributed attractive pinning centers. The presence of a disordered potential forces the system to undergo a transition from a spatially ordered hexagonal state to a spatially disordered one. For both low and high density of pinning centers, we found a continuous transition from an ordered phase to a hexatic phase in which the orientational order parameter describing the local ordering remains nonzero. For the high density of pinning centers the system will also undergo a transition from the hexatic phase to a liquid like phase when the pinning strength is increased. Regarding the dynamical properties of driven overlayers, we have presented the nonlinear response to an external driving force of the most common stable commensurate states, namely the (1×1) and the $c(2 \times 2)$ phases presented. These are particularly interesting cases that may be relevant to other systems such as driven adsorbed monolayers [46, 45, 27], driven charge density waves [23, 38] and driven flux lattices [22, 49]. In general the results of these studies indicate both discontinuous and continuous transitions depending on the magnitude of the pinning strength [38, 36, 6]. For high pinning strengths continuous transitions occurred with the velocity near the transition scaling as $(f - f_c)^{1/2}$, independent of the dimension of the system. This is as expected, since for a commensurate state in a strong periodic pinning potential, each 'particle' acts independently and the model reduces to an effective single particle in a periodic potential, with a known depinning exponent of 1/2. Perhaps more interesting is the observation of discrete transitions and hysteresis loops found at low pinning strengths. While such behavior is expected in the presence of inertial terms both in 1D and 2D, it is quite interesting to see it in 1D, where dislocations are not available, and dynamics being used is overdamped and purely relaxational. It is interesting to speculate that this behavior is intimately related to the need for plastic deformations to mediate the transition from one lattice structure to another. Work on these problems is already in progress.

References

[1] P. B. Littlewood A. A. Middleton, O. Biham and P. Sibani. 1992. Phys. Rev. Lett. 68, page 1586.

[2] S. Sokolowski A. Patrykiejew and K. Binder. 2000. Surf. Sci. Rep. 37, page 207.

[3] X. Duval A. Thomy and J. Regnier. 1980. Surf. Sci. Rep. 1, page 1.

[4] Neil W. Ashcroft and N. David Mermin. 1976. Solid State Physics. Brooks Cole, USA.

[5] P. Bak. 1982. Rep. Prog. Phys. 45, page 587.

[6] L. Balents and M. P. A. Fisher. 1995. Phys. Rev. Lett. 75, page 4270.

[7] K. Binder. 1981. Phys. Rev. Lett. 47, page 693.

[8] K. Binder. 1997. Rep. Prog. Phys. 60, page 487.

[9] C.J. Olson C. Reichhardt and F. Nori. 1998. Phys. Rev. B 58, page 6534.

[10] K. R. Elder E. Granato T. Ala-Nissila C. V. Achim, M. Karttunen and S. C. Ying. 2006. Phys. Rev. E 74, page 021104.

[11] K. R. Elder E. Granato T. Ala-Nissila C. V. Achim, M. Karttunen and S. C. Ying. 2008. J. Phys.: Conf. Ser. 100, page 072001.

[12] M. Karttunen K. R. Elder-E. Granato T. Ala-Nissila C. V. Achim, J. A. P. Ramos and S. C. Ying. 2009. Phys. Rev. E 79, page 011606.

[13] P. M. Chaikin and T. C. Lubensky. 1995. Principles of Condensed Matter Physics. Cambridge University Press, Cambridge, England.

[14] S.N. Coppersmith and D.S. Fisher. 1988. Phys. Rev. A 38, page 6338.

[15] J.C. Crocker and D.G. Grier. 1996. J. Colloid Interface Sci. 179, page 298.

[16] P. Le Doussal and T. Giamarchi. 1998. Phys. Rev. B 57, page 11356.

[17] K. R. Elder. and M. Grant. 2004. Phys. Rev. E 70, page 051605.

[18] E. Fawcett. 1988. Rev. Mod. Phys. 60, page 209.

[19] P. Bak F.D.M. Haldane and T. Bohr. 1983. Phys. Rev. B 28, page 2743.

[20] D. S. Fisher. 1983. Phys. Rev. Lett. 50, page 1486.

[21] D. S. Fisher. 1985. Phys. Rev. B 31, page 1396.

[22] V. B. Geshkeibein A. I. Larkin G. Blatter, M. V. Feigel'man and V. M. Vinokur. 1994. Rev. Mod. Phys 66, page 1125.

[23] A Zawadowski G. Grüner and P. M. Chaikin. 1981. Phys. Rev. Lett. 46, page 511.

[24] Nigel Goldenfeld. 1976. Lectures on Phase Transitions and the Renormalization Group. Brooks Cole, USA.

[25] E. Granato. 2008. Phys. Rev. Lett. 101, page 027004.

[26] E. Granato and S. C. Ying. 1999. Phys. Rev. B 59, page 5154.

[27] E. Granato and S.C. Ying. 2000. Phys. Rev. Lett. 85, page 5368.

[28] K. Hukushima and K. Nemoto. 1996. J. Phys. Soc. Jpn. 65, page 1604.

[29] C. V. Achim S. C. Ying-K. R. Elder J. A. P. Ramos, E. Granato and T. Ala-Nissila. 2008. Phys. Rev. E 78, page 031109.

[30] J. Nogués J. I. Martí n, M. Vélez and I. K. Schuller. 1997. Phys. Rev. Lett. 79, page 1929.

[31] J. Jalkanen. 2006. Private communication.

[32] C.V. Achim M. Karttunen S.C. Ying K.R. Elder J.A.P. Ramos, E. Granato and T. Ala-Nissila. Unpublished.

[33] A. Jaster. 2004. Phys Lett A 330, page 120.

[34] M. Katakowski K. R. Elder, M. Haataja, and M. Grant. 2007. Phys. Rev. B 75, no. 6, page 064107.

[35] M. Haataja K. R. Ken, M. Katakowski and M. Grant. 2002. Phys. Rev. Lett. 88, no. 24, page 245701.

[36] Y. Li J.D. Brock S.G. Lemay K.L. Ringland, A.C. Finnefrock and R.E. Thorne. 1999. Phys. Rev. Lett 82, page 1923.

[37] T. A. Kontorova and Y. I. Frenkel. 1939. Zh. Eksp. Teor. Fiz. 8, page 89.

[38] K. R. Elder M. Karttunen, M. Haataja and M. Grant. 1999. Phys. Rev. Lett 83, page 3518.

[39] E. Marinari and G. Parisi. 1992. J. Phys. Soc. Jpn. 19, page 451.

[40] Gene F. Mezenko. 2003. Fluctuations, order and defects. Wiley VCH, New Jersey, USA.

[41] A. A. Middleton and D. S. Fisher. 1991. Phys. Rev. Lett. 66, page 92.

[42] C. R. Myers and J. P. Sethna. 1993. Phys. Rev. B 47, page 11171.

[43] M. Haataja P. Stefanovic and N Provatas. 2006. Phys. Rev. Lett. 96, page 225504.

[44] M. Patra and M. Karttunen. 2006. Numerical Methods for Partial Differential Equations 22, page 936.

[45] B. N. J. Persson. 1993. Phys. Rev. B 71, page 1212.

[46] B.N.J. Persson. 1998. Sliding Friction: Physical Principles and Applications. Springer, Heidelberg, Germany.

[47] L. F. Schneemeyer R. M. Fleming and D. E. Moncton. 1985. Phys. Rev. B 31, page 899.

[48] M. Schick R. Pandit and M. Wortis. 1982. Phys. Rev. B. 26, page 5112.

[49] C. Reichhardt and F. Nori. 1999. Phys. Rev. Lett. 82, page 414.

[50] F.S. Rys. 1983. Phys. Rev. Lett. 51, page 849.

[51] M. Schick. 1981. Prog. Surf. Sci. 11, page 245.

[52] Y. Singh. 1991. Phys. Rep. 207, page 351.

[53] P. F. Tua and J. Ruvalds. 1985. Phys. Rev. B 32, page 4660.

[54] K. A. Wu and A. Karma. 2007. Phys. Rev. B 76, page 184107.

Appendix A Derivation of the PFC model from the DFT theory of freezing

In this section it is shown how the free energy of a pure system is obtained as an approximation of the classical DFT of freezing following the calculations done by *Elder et al.* [34]. In the classical DFT of freezing [52] the free energy of the solid phase is written as perturbation around a reference liquid state at the melting transition

$$\begin{aligned} \mathcal{F}_{\text{DFT}}/k_BT &= \int d\vec{x}\,[\rho(\vec{x})\log(\rho(\vec{x})/\rho_l) - \delta\rho(\vec{x})] \\ &- (1/2)\int d\vec{x}d\vec{x}'\delta\rho(\vec{x})C(\vec{x}-\vec{x}')\delta\rho(\vec{x}'), \end{aligned} \tag{A.1}$$

where $C(\vec{x}-\vec{x}')$ is the direct two point correlation function in reference liquid. In order to understand basic features of this free energy functional it is useful to expand $\mathcal{F}_{\text{DFT}}$ around the average density, $\bar{\rho}$, using the rescaled density

$$n(\vec{x}) = \frac{\rho(\vec{x})-\bar{\rho}}{\bar{\rho}}. \tag{A.2}$$

Expanding the nonlinear part of $\mathcal{F}_{\text{DFT}}$ in powers of n gives

$$\begin{aligned} \frac{\mathcal{F}_{\text{DFT}}}{\bar{\rho}k_BT} &= \int \vec{x}\left(\frac{n^2}{2} - \frac{n^3}{6} + \frac{n^4}{12} + \cdots\right) \\ &- \frac{\bar{\rho}}{2}\int d\vec{x}d\vec{x}'n(\vec{x})C(\vec{x}-\vec{x}')n(\vec{x}') + \frac{\mathcal{F}^0_{\text{DFT}}}{\bar{\rho}k_BT}, \end{aligned} \tag{A.3}$$

where $\frac{\mathcal{F}^0_{\text{DFT}}}{\bar{\rho}k_BT}$ is the free energy of a liquid with average density $\bar{\rho}$. The contribution from the correlation function can be written as $\bar{\rho}\sum_{\vec{k}}\hat{n}(\vec{k})\hat{c}(\vec{k})\hat{n}(-\vec{k})$, with the Fourier transforms of the rescaled density and correlation function $\hat{n}(\vec{k}) = \int d\vec{x}e^{i\vec{k}\cdot\vec{x}}n(\vec{x})$ and $\hat{c}(\vec{k}) = \int d\vec{x}e^{i\vec{k}\cdot\vec{x}}c(\vec{x})$. Next the Fourier transforms of the two point correlation is approximated with a forth order polynomial which has only even powers

$$\hat{c}(\vec{k}) = \hat{C}_0 + \hat{C}_2k^2 + \hat{C}_4k^4. \tag{A.4}$$

The coefficients $\hat{C}_0, \hat{C}_2$ and $\hat{C}_4$ are fitted then to the position (k_m), height ($\hat{c}_m$) and second derivative of the first maximum of the two point correlation function of the material of interest (see Fig. A.1 for an example).

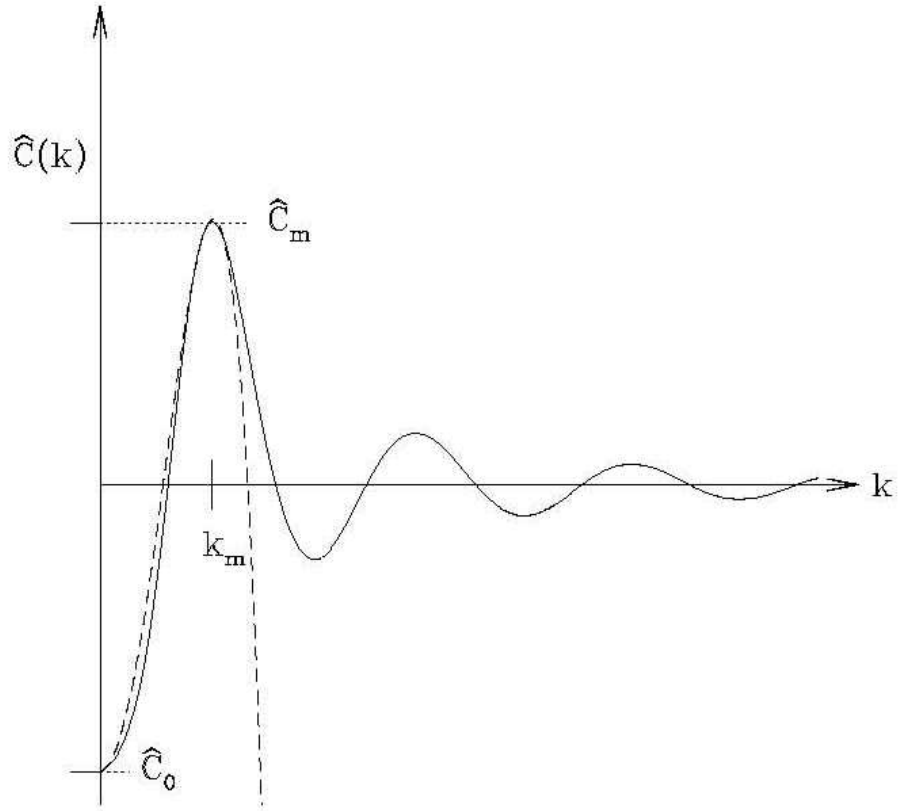

Figure A.1: A typical liquid state two-point direct correlation function is sketched. The dashed line represents one of the possible approximations of the liquid two point correlation function, as presented in Ref. [34].

In real space the approximation given by Eq. (A.4) corresponds to $C(\vec{x}-\vec{x}') = (\hat{C}_0 - \hat{C}_2\nabla + \hat{C}_4)\delta(\vec{x}-\vec{x}')$. Taking into account the approximations done and restricting the expansion of the log term to the forth power, the condensation energy of the system can be written as

$$\begin{aligned} F_{\text{DFTPFC}} &= \frac{\mathcal{F}_{\text{DFT}} - \mathcal{F}^0_{\text{DFT}}}{k_B T} \\ &= \bar{\rho}\int d\vec{x}\left(\frac{B_l}{2}n^2 + \frac{B_s}{2}n\left(2R^2\nabla^2 + R^4\nabla^4\right)n - \frac{n^3}{6} + \frac{n^4}{12}\right), \end{aligned} \tag{A.5}$$

where $B_l = 1 - \bar{\rho}\hat{C}_0$ is related to the isothermal compressibility in the liquid phase, $B_s = \bar{\rho}(\hat{C}_2^2)/(|\hat{C}_4|)$ is related to the bulk modulus of the crystal and $1/R = \sqrt{\hat{C}_2/(2\hat{C}_4)}$ gives the magnitude of the first reciprocal lattice vector and implicit the lattice constant.

Comparing Eq. (A.5 with Eq. (2.3) it is obvious that they are the same up to some additive constant. In order to prove we rescale the adimensional density field of the SHPFC model,

$$\psi(\vec{x}) = R_1 n(\vec{x}) + \bar{\psi}. \tag{A.6}$$

The constant R_1 and the relationship between the different parameters of the two forms of the free energy can be determined by comparing coefficients of each term in Eqs. (A.5) and (2.3). With the rescaled density and taking into account that $\int d\vec{x} n(\vec{x}) = 0$ the free energy of the SHPFC model is

$$F_{\text{SHPFC}} = \int \left(\frac{R_1^2}{2} n(r + k_0^4 + 6\bar{\psi}^2)n + \frac{R_1^2}{2} n(2k_0^2\nabla^2 + \nabla^4)n + \frac{R_1^4}{4} n^4 + R_1^3 \bar{\psi} n^3 \right) + F_c, \tag{A.7}$$

where F_c is the free energy of the liquid given by (2.6). From Eqs. (A.7) and (A.5) it can be seen that $F_{\text{DFTPFC}} \equiv F_{\text{SHPFC}} - F_c$ if

$$\begin{aligned} \bar{\rho} B_l &= R_1^2 (r + k_0^4 + 6\bar{\psi}^2) \\ \bar{\rho} B_s R^2 &= R_1^2 k_0^2 \\ \bar{\rho} B_s R^4 &= R_1^2 \\ \bar{\rho}/3 &= R_1^4 \\ -\bar{\rho}/6 &= R_1^3 \bar{\psi} \end{aligned} \tag{A.8}$$

These set of equations can be easily solved and the results are

$$R_1 = -\frac{\bar{\psi}}{2}, \bar{\rho} = \frac{3}{16}\bar{\psi}^4, 1/R = k_0, B_s = \frac{4k_0^4}{3\bar{\psi}^2}, B_l = \frac{4}{3\bar{\psi}^2}(r + k_0^4 + 6\bar{\psi}^2). \tag{A.9}$$